Naval Research Laboratory
Washington, DC 20375-5320

NRL/7260/FR--2024/1

Polarimetric Analysis of Bistatic Synthetic Aperture Radar Imagery: Final Report

YANTING WANG
MARK A SLETTEN

Image Science and Applications Branch
Remote Sensing Division

April 12, 2024

REPORT DOCUMENTATION PAGE

PLEASE DO NOT RETURN YOUR FORM TO THE ABOVE ORGANIZATION

1. REPORT DATE	2. REPORT TYPE	3. DATES COVERED	
		START DATE	END DATE
April 12, 2024	Formal Report	October 1, 2018	September 30, 2023

4. TITLE AND SUBTITLE

Polarimetric Analysis of Bistatic Synthetic Aperture Radar Imagery: Final Report

5a. CONTRACT NUMBER	5b. GRANT NUMBER	5c. PROGRAM ELEMENT NUMBER
		0601153N
5d. PROJECT NUMBER	**5e. TASK NUMBER**	**5f. WORK UNIT NUMBER**
	BE032-08-41	991L27

6. AUTHOR(S)

Yanting Wang, Mark A Sletten

7. PERFORMING ORGANIZATION / AFFILIATION NAME(S) AND ADDRESS(ES)

U. S. Naval Research Laboratory
4555 Overlook Avenue, SW
Washington, DC 20375

8. PERFORMING ORGANIZATION REPORT NUMBER

NRL/7260/FR--2024/1

9. SPONSORING / MONITORING AGENCY NAME(S) AND ADDRESS(ES)	10. SPONSOR / MONITOR'S ACRONYM(S) NUMBER	11. SPONSOR / MONITOR'S REPORT NUMBER(S)
	NRL	

12. DISTRIBUTION / AVAILABILITY STATEMENT

DISTRIBUTION STATEMENT A: Approved for public release; distribution is unlimited.

13. SUPPLEMENTAL NOTES

14. ABSTRACT

This report documents the outcomes for an NRL 6.1 Base Program project towards developing the polarimetric techniques for the analysis of bistatic synthetic aperture radar imagery. Bistatic polarimetric radar collects additional scattering information with more degrees of freedom than monostatic polarimetric radar. In this program, we explore the potential advantages of using bistatic polarimetric observations for remote sensing applications. We present the physical foundation geared toward bistatic imagery interpretation and the fundamental challenge induced by the entangled bistatic geometry. The analysis is formed on the bistatic scattering models and characterization of several common scattering mechanisms, such as double-bounce scattering, surface scattering, and random volume scattering. We develop target decomposition and parameter estimation algorithms to demonstrate the enhanced utility of bistatic polarimetric imagery. Bistatic data collection can be costly and demands extra mission planning; concerning this, we present a sensitivity study to address the optimal choice of bistatic imaging geometries for soil moisture retrievals.

15. SUBJECT TERMS

Synthetic Aperture Radar, Polarimetry, Bistatic

16. SECURITY CLASSIFICATION OF:			17. LIMITATION OF ABSTRACT	18. NUMBER OF PAGES
a. REPORT	b. ABSTRACT	c. THIS PAGE		
U	U	U	UU	47

19a. NAME OF RESPONSIBLE PERSON	19b. PHONE NUMBER *(Include area code)*
Yanting Wang	202-767-8248

This page intentionally left blank

CONTENTS

1 INTRODUCTION 1
1.1 Background and Motivation 1
1.2 Technical Challenges 1
1.2.1 Geometry Coupling 1
1.2.2 Polarimetric Decomposition 2
1.2.3 Bistatic Scattering Signatures 3
1.2.4 Collection Configurations 4
2 POLARIMETRY FUNDATION FOR BISTATIC SCATTERING 4
2.1 The Reciprocity Theorem and Bistatic Scattering Matrix 4
2.2 The Standard Reference System and Basis 5
2.3 The Characteristic Properties 6
3 BISTATIC SCATTERING MODELS 8
3.1 Rayleigh Dielectric Sphere 8
3.2 Specular Scattering 10
3.3 Double-Bounce Scattering 11
3.4 Surface Scattering 14
3.5 Volume Scattering 15
4 POTENTIAL APPLICATIONS 18
4.1 Scatter Parameter Estimation 18
4.1.1 Specular Scattering Parameters 18
4.1.2 Dihedral Scattering Parameters 18
4.1.3 Surface Scattering Parameters 19
4.2 Polarimetric Interpretation and Target Decomposition 21
4.2.1 Eigenvector-Based Decomposition 21
4.2.2 Model-Based Decomposition 22
4.2.3 Shape Adaptive Vegetation Scatter Model 23
4.3 Rough Surface Scattering and Parameter Estimation 25
4.3.1 Extended-Bragg Scattering Model 25
4.3.2 Two-Scale Rough Surface Scattering Model 26
4.3.3 Rough Surface Parameter Estimation 28
5 SENSITIVITY AND IMAGING GEOMETRY 31
6 CONCLUSIONS 36
REFERENCES 36

FIGURES

Fig. 1—A typical bistatic SAR configuration in which either the transmitter or the receiver is installed on a moving platform with the other kept stationary. The beam direction is specified in a pair of orientation angles including zenith angle θ and azimuth angle ϕ. The EM wave is specified in a right-hand triplet of wavevector k and polarization vectors v and h. 2

Fig. 2—Beam geometry and polarization reference system: (a) the native observation system; (b) the standard bistatic reference system with the bisector vector b defined as Z-axis. The bistatic angle equals to 2η. 6

Fig. 3—The characteristic polarization parameters of dielectric sphere scattering at varying receiving directions: (a) incidence side polarization rotation; (b) scattering side polarization rotation; (c) inter-polarization scattering ratio; (d) the skip angle. The symbol "+" marks for the fixed incidence direction and the symbol "x" marks for the specular scattering direction. The scattering wave is received at varying direction in the upper hemisphere, with the radius measuring the zenith angle and the concentric locations measuring the azimuth angle. 9

Fig. 4—Same as Fig.3 except for the characteristic polarization parameters of specular scattering. The positions in the plots indicate the surface normal direction, effectively varying the receiving directions. 11

Fig. 5—The dependence of (a) the scattering ratio and (b) the skip angle on the bistatic angle and the relative permittivity. The skip angle can change at a bistatic setting related to the permittivity 11

Fig. 6—Diagram of a dihedral reflector with one of the two double-bounce scattering paths 12

Fig. 7—The bistatic double-bounce scattering signature of a dihedral corner reflector at changing incidence angle (η) and dihedral orientation angle (θ) 13

Fig. 8—Same as Fig.3 except for the characteristic polarization parameters of a slightly rough, horizontal surface scattering at varying receiving directions. Panels (c) and (d) show the small but nonzero ellipticity angles. 15

Fig. 9—(a) A spheroid with the symmetric axis oriented at (θ, ϕ); (b) a random volume of vegetation scatterers 16

Fig. 10—The varying difference between the inter-channel correlation coefficients of random disk scatter and random needle scatter at different bistatic angles 17

Fig. 11—The errors on the estimated permittivity, different between the two dihedral facets, under known rotation angles 19

Fig. 12—The errors on the estimated rotation angle (a) and on the estimated permittivity, shared between the two dihedral facets (b) 19

Fig 13—The errors on the estimated surface parameters using bistatic observations: (a) surface permittivity, and (b) zenith angle and (c) azimuth angle of the surface normal vector. The symbol "+" marks the incidence direction and the symbol "Δ" marks the normal vector direction. The positions in the plots indicate the scattering direction at reception. 20

Fig 14—Same as Fig. 13, except for the estimation using joint bistatic and monostatic observations 21

Fig 15—The radar beam is incident from the top of the image. Test site imagery: (a) F-SAR image in Pauli-basis pseudocolor composition, and (b) the collocated optical image. 24

Fig. 16—The marginal distribution of POA (left) and LIA (right) incurred by random surface orientation. The orientation distribution follows a vMF distribution with $\kappa = 20$. The line colors mark for different radar look angles. 26

Fig. 17—The $\rho 4$- ALF space of varying orientation randomness and varying relative permittivity, when (a) the LIA variation is not accounted for, (b) the LIA variation is accounted for Guassian roughness spectrum (L = 0.1λ), and (c) the LIA variation is accounted for fractal roughness spectrum (Hurst exponent = 0.8)..... 28

Fig. 18—(a) L-band UAVSAR image near Camp Roberts, California, color-coded in the Pauli basis, (b) the co-registered SRTM DEM map, (c) the derived polarization orientation angles. From top to bottom is the slant range direction. 29

Fig. 19—The mean POA maps estimated from $T23$-POA (a) and $T13$-POA (b); and the density distribution between the DEM-derived POA (x-axis) and the estimated POA (y-axis) using $T23$-POA (c) and $T13$-POA (d) 30

Fig. 20—The magnitude of estimated εr based on the X-Bragg model with the LIA variation ignored (a) and with the LIA variation incorprated (b). The dark-blue color indicates invalid solution to the scattering models..... 31

Fig. 21—Sensitivity evaluation on the normalized scattering intensities: (a) the changes due to SMC increases; (b) the quality factor $ISM - L$; (c) the quality factor $ISM - \kappa$. 33

Fig. 22—Sensitivity evaluation on the scattering intensity ratios: (a) the changes due to SMC increases; (b) the quality factor $ISM - L$; (c) the quality factor $ISM - \kappa$. 34

Fig. 23—Sensitivity evaluation on the characteristic polarization angles: (a,b) the changes due to SMC increases; (c,d) the quality factor $ISM - L$; (e,f) the quality factor $ISM - \kappa$. 35

Fig. 24—Sensitivity evaluation on the characteristic scattering ratio: (a) the changes due to SMC increases; (b) the quality factor $ISM - L$; (c) the quality factor $ISM - \kappa$. 36

This page intentionally left blank

EXECUTIVE SUMMARY

Bistatic radar has recently been gaining revived interest in many fields of remote sensing and target detection. Particularly, bistatic synthetic aperture radar (BiSAR) offers an attractive imaging mode by removing the restrictive monostatic imaging geometry. When equipped with a multipolarization configuration, it also allows imagery collection of additional scattering information with more degrees of freedom than those of monostatic observation. Several BiSAR systems have been built with the ability to operate with multiple polarization channels.

Our focus in this program was to explore the potential advantages of acquiring polarimetric BiSAR imagery. Polarimetric analysis and processing approaches are well established in the monostatic sensing paradigm. However, this knowledge is not directly applicable to BiSAR imagery and we need to build the essential foundation for bistatic polarimetric techniques.

The polarimetric analysis in the early development was based primarily on mathematical manipulation of the bistatic scattering matrix. There exists a significant gap between polarimetric imagery acquisition and physical target inference. Through this work, we laid out the physical foundation geared toward bistatic imagery interpretation. We explicitly developed the constraint on the bistatic scattering matrix and the geometry factors in the polarimetric observations. We expressed the coupling effect due to sensing geometries that, if not compensated, would induce a systematic polarization orientation on the polarimetric scattering response.

We established the analytic construct for geometry compensation and intrinsic polarimetric parameter derivation. With those, we developed the bistatic scattering models of several common scattering mechanisms, particularly including double-bounce scattering, surface scattering, and random volume scattering. We evaluated their polarimetric characteristics under general imaging geometries that would be used to drive target characterization and imagery interpretation.

As a major effort, we explored the potential utility of bistatic polarimetric SAR imagery. The additional polarization channel, which is associated with the asymmetry of the bistatic scattering matrix, indeed gives us an important advantage in estimating the target parameters. A complete determination is not possible using monostatic polarimetric observation. In particular, we exploited the synergy between bistatic observation and the simultaneous monostatic observation to improve the estimation of surface orientation angles. We developed the fundamental, physical-based target decomposition technique. Intended for rough terrain surface and soil moisture application, we developed the scattering models that are able to account for the random orientation variation incurred by increased roughness but also to facilitate polarization basis transformation.

Lacking real bistatic imagery, we applied the new development to legacy monostatic polarimetric SAR datasets when possible. We improved forest scene description with adaptability to different vegetation scatter types, and polarization orientation angle and soil moisture estimation in steep mountainous terrain. BiSAR collection can be costly and demands extra mission planning; concerning this, we established a process to address the optimal choice of bistatic imaging geometries for soil moisture retrievals.

This page intentionally left blank

POLARIMETRIC ANALYSIS OF BISTATIC SYNTHETIC APERTURE RADAR IMAGERY: FINAL REPORT

1 INTRODUCTION

1.1 Background and Motivation

Bistatic synthetic aperture radar (BiSAR) presents an attractive radar imaging option by pairing a passive receiver with a remotely separate active transmitter [1,2]. Using a passive receiver can make the sensor system smaller and the covert operation in a hostile environment possible. The separate active transmitter can be either dedicated, opportunistic, or even noncooperative. Furthermore, the BiSAR imagery can be formed in any direction around the receiver, removing the restrictive imaging geometry of a monostatic SAR system. From the perspective of remote sensing, BiSAR collects target responses of various scattering behaviors, including those of forward scattering, with potential enhancement over monostatic SAR's backscattering data.

However, both the implementation of a bistatic system and the interpretation of the bistatic observations face many challenges; as a result, bistatic radar is not widely deployed in practice and its development went through several resurgences [3,4]. In this program, our focus was devoted to the exploitation of the additional information content contained in the BiSAR imagery for sensing applications. Particularly, we intended to explore the polarimetry capability under the bistatic sensing paradigm.

In theory, data acquired through multiple polarization channels would carry a rich set of target information. Radar polarimetry with a monostatic SAR offers important sensing advantages to infer geophysical parameters such as size, shape, and orientation of the ground targets as well as the underlying scattering mechanism [5]. Analytic techniques are well established for polarimetric monostatic SAR to characterize targets according to their polarimetric signatures [6]. However, the theoretical link between polarimetric BiSAR observations and the target-scattering properties is currently absent for physical interpretation [7]. Through this program, we create the fundamental foundation for bistatic scattering characterization and polarimetric analysis. With a better understanding of target features amid natural clutter in the BiSAR imagery, ultimately, we hope to make improvement on scene classification, target detection, and clutter suppression by taking advantage of the unrestricted bistatic imaging configurations.

1.2 Technical Challenges

1.2.1 Geometry Coupling

While BiSAR enables flexible imaging geometries, the sensing geometry is also deeply coupled in the scattering response. On the one hand, the scattering process can change at different geometric configurations, for example, varying from backscattering to forward scattering. This varying presence creates a barrier to BiSAR polarimetric analysis. On the other hand, the polarization states used in the

Manuscript approved April 10, 2024.

BiSAR system will also continuously evolve with the sensing geometry, imposing an additional polarization rotation on the scattering response. The fact that the transmitter and the receiver operate in different polarization bases needs to be correctly accounted for in the polarimetric analysis.

Figure 1 illustrates a generic bistatic imaging setup by pairing a moving radiator with a stationary receiver. The incident wave comes from the direction (θ_i, ϕ_i); the receiver probes the scattered wave at the direction (θ_s, ϕ_s). Reference of the polarization states in the sensing system is based on the following wave triplets:

$$\hat{h}_p = \hat{Z} \times \frac{\hat{k}_p}{\sin\theta_p}, \tag{1}$$

$$\hat{v}_p = \hat{h}_p \times \hat{k}_p, \tag{2}$$

where $\hat{Z}$ is the vertical direction, $\hat{k}$ denotes the wave propagation direction, and p labels the incidence or scattering association with either "i" or "s". Accordingly, we can find the angles between the polarization states at the separate transmitter and receiver locations evolving as

$$\angle h_i, h_s = \pi - (\phi_i - \phi_s), \tag{3}$$

$$\angle v_i, v_s = \cos^{-1}[\cos\theta_i \cos\theta_s \cos(\phi_i - \phi_s) + \sin\theta_i \sin\theta_s]. \tag{4}$$

The difference between the polarization states is significant because the observed scattering matrix should be interpreted within the context of the specific polarization combination. In addition, for most scenarios, the one in the transmitter and the one in the receiver do not align in the same direction; thus, usage of "copolar" or "cross-polar" can be ill-advised.

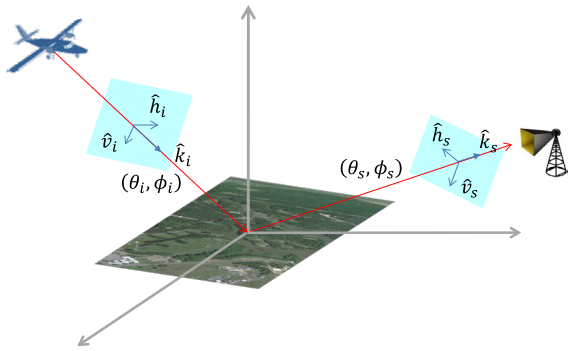

Fig. 1—A typical bistatic SAR configuration in which either the transmitter or the receiver is installed on a moving platform with the other kept stationary. The beam direction is specified in a pair of orientation angles including zenith angle θ and azimuth angle ϕ. The EM wave is specified in a right-hand triplet of wavevector $\hat{k}$ and polarization vectors $\hat{v}$ and $\hat{h}$.

1.2.2 Polarimetric Decomposition

The freedom of choosing various imaging geometries comes at the cost of analytic complexity of the target-scattering matrix. In the monostatic case, the radar operates in the same polarization basis and the scattering matrix is known to be symmetric when the backscattering alignment (BSA) is adopted [8,9]. In the bistatic case, the scattering matrix defines a generic linear map from the incident polarization basis to the scattering polarization basis, which is not symmetric [10].

The nonsymmetry in the scattering matrix may be regarded as a potential augmentation of the scatter information content. However, symmetry is the fundamental assumption underlying the existing polarimetric analysis techniques [11]. One treatment for nonsymmetric scattering matrices is to decompose them into symmetric and skew-symmetric components [12–14]. While this mathematically allows the existing techniques to be operable, the relevant physical implications are not clear from such decompositions.

When the common Pauli decomposition is applied, the decomposition basis is expanded, including the skew-symmetric component, into four channels:

$$\begin{bmatrix}1 & 0\\ 0 & 1\end{bmatrix}, \begin{bmatrix}1 & 0\\ 0 & -1\end{bmatrix}, \begin{bmatrix}0 & 1\\ 1 & 0\end{bmatrix}, \begin{bmatrix}0 & i\\ -i & 0\end{bmatrix}. \tag{5}$$

This induces a false implication that the common Pauli decomposition can be used and interpreted in a similar manner. For example, the first channel would widely be used to represent a roll-invariant component, immune to changes of polarization orientation. In the bistatic case, however, the polarization orientation is effected through the following transformation:

$$\mathbf{S} = \begin{bmatrix}\cos\alpha_s & -\sin\alpha_s\\ \sin\alpha_s & \cos\alpha_s\end{bmatrix} \mathbf{S}_0 \begin{bmatrix}\cos\alpha_i & \sin\alpha_i\\ -\sin\alpha_i & \cos\alpha_i\end{bmatrix}, \tag{6}$$

where α_i and α_s are the polarization rotation angles. Then, the first Pauli component can be derived from

$$\left\langle \begin{bmatrix}1 & 0\\ 0 & 1\end{bmatrix}, \mathbf{S} \right\rangle = \left\langle \begin{bmatrix}\cos(\alpha_i-\alpha_s) & -\sin(\alpha_i-\alpha_s)\\ \sin(\alpha_i-\alpha_s) & \cos(\alpha_i-\alpha_s)\end{bmatrix}, \mathbf{S}_0 \right\rangle, \tag{7}$$

which obviously is not roll-invariant unless $\alpha_i = \alpha_s$. For the monostatic case, we know $\alpha_i = \alpha_s$ because of the symmetric scattering matrix; hence, the roll-invariant property stands. This is not the case with a bistatic scattering matrix for which α_i and α_s are not necessarily equal; accordingly, Pauli decomposition loses its advantage and it should not be interpreted in the same monostatic way.

1.2.3 Bistatic Scattering Signatures

Many targets can be considered as an aggregation of several standard scatterers. It is easier to analyze and characterize each basic scattering element than the complex targets as a whole. In the monostatic paradigm, scattering elements include spheres, flat plates, dihedrals, dipoles, helices, wires, and cylinders. The backscatter matrix is commonly decomposed as a combination of single-bounce, double-bounce and volume-scattering mechanisms and then is mapped into these basic scatter types [5, 11]. The standard single-bounce signature and the standard double-bounce signature are orthogonal. In the bistatic paradigm, those standard scatterers behave differently depending upon the bistatic angles, formed between the incidence and scattering directions. This makes the determination of the canonical scattering mechanisms more convolved. We need to develop the general bistatic scattering models and to characterize the bistatic scattering signatures amid arbitrary imaging geometries to create the necessary building blocks for the bistatic polarimetric analysis.

Characterization of the characteristic scattering components from the nonsymmetric bistatic scattering matrices requires two pairs of polarization bases, one set for the incidence side and another for the scattering side [10]. The orientation angles of the characteristic polarization states are further dependent on the adopted reference system due to the coupled geometry factor. Moreover, the relative phase information between the characteristic components needs to be properly retained to express the involved scattering mechanism.

1.2.4 Collection Configurations

While using BiSAR opens up the imaging geometry, it also introduces an extra system design parameter important to data collection. A bistatic imaging system can be formed from two moving platforms, one for the transmitter and the other for the receiver. The movement and the beam directions will define the imagery resolution. The beam geometry also controls what scattering process is being probed and accordingly determines the information content. These are the additional system variables to be carefully considered during mission planning for the optimal collection of the scattering observations.

Even if one of the platforms is kept stationary, as shown in Fig.1, we still face numerous options to point the antenna toward different directions because we will expect to receive different kinds of scattering phenomena and data quality. For example, acquisition at backscatter directions may not give us additional information content, whereas acquisition at the specular direction may have limited field of view and poorer resolution [15]. Based on the problem at hand, we want to explore the favorable sensing geometry for acquisition of the physical target properties.

2 POLARIMETRY FUNDATION FOR BISTATIC SCATTERING

2.1 The Reciprocity Theorem and Bistatic Scattering Matrix

In a bistatic sensing system, suppose the incident wave propagates toward a target along direction $\hat{k}_i$ and the scattered wave is observed at direction $\hat{k}_s$. The incident electric field has a magnitude of E_0 and a polarization state of $\hat{q}$, resulting in a scattered electric field $\vec{E}_s(\hat{k}_i, \hat{q}; \hat{k}_s)$.

Consider the case where all the propagation directions are reversed. The incident wave propagates toward the target along direction $-\hat{k}_s$, having a magnitude of E_0 and a polarization state of $\hat{t}$. The resulting scattered electric field is noted as $\vec{E}_s(-\hat{k}_s, \hat{t}; -\hat{k}_i)$.

Following the reciprocity theorem [16], we have

$$\hat{t} \cdot \vec{E}_s(\hat{k}_i, \hat{q}; \hat{k}_s) = \hat{q} \cdot \vec{E}_s(-\hat{k}_s, \hat{t}; -\hat{k}_i). \tag{8}$$

This relation imposes a constraint between the bistatic scattering matrices of these two cases. In the former case, we define the scattering matrix $[\mathbf{S}_F]$ relating the incident polarization basis $(\hat{p}, \hat{q})$ to the scattered polarization basis $(\hat{s}, \hat{t})$. The polarization bases are specified in a way to satisfy the orthogonal wave triplets of the forward scatter alignment (FSA), namely $\hat{q} \times \hat{p} = \hat{k}_i$ and $\hat{t} \times \hat{s} = \hat{k}_s$ [17]. In the latter case, we define the scattering matrix $[\mathbf{S}_R]$ relating the incident polarization basis $(\hat{s}, -\hat{t})$ to the scattered polarization basis $(\hat{p}, -\hat{q})$; the additional negative sign in the polarization bases are introduced to satisfy the same FSA triplets under the reversed propagation directions.

The scattered electric fields can be written in terms of the scattering matrix elements as:

$$\vec{E}_s(\hat{k}_i, \hat{p}; \hat{k}_s) = E_0(S_{F11}\hat{s} + S_{F21}\hat{t}), \tag{9}$$
$$\vec{E}_s(\hat{k}_i, \hat{q}; \hat{k}_s) = E_0(S_{F12}\hat{s} + S_{F22}\hat{t}), \tag{10}$$
$$\vec{E}_s(-\hat{k}_s, \hat{s}; -\hat{k}_i) = E_0(S_{B11}\hat{p} - S_{B21}\hat{q}), \tag{11}$$
$$\vec{E}_s(-\hat{k}_s, \hat{t}; -\hat{k}_i) = -E_0(S_{B12}\hat{p} - S_{B22}\hat{q}). \tag{12}$$

Replacing Eqs. (10) and (12) in Eq. (8) leads to the equality $S_{F22} = S_{B22}$. Similarly, we can find $S_{F11} = S_{B11}$ using Eqs. (9) and (11), $S_{F21} = -S_{B12}$ using Eqs. (9) and (12), and $S_{F12} = -S_{B21}$ using Eqs. (10) and (11). This set of the relations derived from the reciprocity theorem can serve as a fundamental check on the developed bistatic scattering models. For monostatic scattering, $[\mathbf{S}_F]$ and $[\mathbf{S}_B]$ are referred to the same scattering process; thus we reach the special monostatic relation: $S_{F21} = -S_{F12}$.

Note that in the backscatter alignment (BSA), the reference wave vectors are always defined as the directions pointing toward the target [17]. In this convention, no sign change is needed to maintain the orthogonal wave triplets. We can rewrite Eqs. (9)–(12) as:

$$\vec{E}_s(\hat{k}_i, \hat{p}; \hat{k}_s) = E_0(S_{F11}\hat{s} + S_{F21}\hat{t}), \tag{13}$$
$$\vec{E}_s(\hat{k}_i, \hat{q}; \hat{k}_s) = E_0(S_{F12}\hat{s} + S_{F22}\hat{t}), \tag{14}$$
$$\vec{E}_s(-\hat{k}_s, \hat{s}; -\hat{k}_i) = E_0(S_{B11}\hat{p} + S_{B21}\hat{q}), \tag{15}$$
$$\vec{E}_s(-\hat{k}_s, \hat{t}; -\hat{k}_i) = E_0(S_{B12}\hat{p} + S_{B22}\hat{q}). \tag{16}$$

It can be then determined that $[\mathbf{S}_F] = [\mathbf{S}_B]^T$. For monostatic scattering, this, as expected, prescribes a symmetric backscattering matrix.

2.2 The Standard Reference System and Basis

In order to minimize the impact of the polarization difference incurred by the imaging geometry, we can define a new polarization reference system, as shown in Fig. 2. This reference frame is centered on the bistatic plane that contains both the incidence direction and the scattering direction. A common horizontal polarization is then defined as the direction orthogonal to the bistatic plane and the vertical polarization is accordingly defined inside the bistatic plane. They are evaluated as:

$$\hat{H} = \hat{k}_s \times \hat{k}_i / \sin\beta, \tag{17}$$
$$\hat{V}_i = \hat{H} \times \hat{k}_i, \tag{18}$$
$$\hat{V}_s = \hat{H} \times \hat{k}_s, \tag{19}$$

where β stands for the bistatic angle formed between $-\hat{k}_i$ and $\hat{k}_s$ such that it satisfies

$$\cos\beta = -\hat{k}_i \cdot \hat{k}_s. \tag{20}$$

We use this as the standard reference system in our analysis along with its associated polarization bases. Its adoption leads to several important merits: a common $\hat{H}$ shared by both the incident and scattered waves, the orthogonality maintained between $\hat{H}$ and $\hat{V}_{i,s}$, and the presence of relation $\hat{V}_i \cdot \hat{V}_s = -\cos\beta$. In some sense, we mitigate the geometry dependence to the utmost degree and reestablish the cross-polarization channels in the scattering analysis.

The transformation between the native polarization system, $\{h_i, v_i\}$ and $\{h_s, v_s\}$, and the standard reference system, $\{H, V_i\}$ and $\{H, V_s\}$, can be readily attained by applying the following polarization rotation operation:

$$\mathbf{S}_{\{H,V\}} = \begin{bmatrix} \hat{H}\cdot\hat{h}_s & \hat{H}\cdot\hat{v}_s \\ \hat{V}_s\cdot\hat{h}_s & \hat{V}_s\cdot\hat{v}_s \end{bmatrix} \mathbf{S}_{\{\boldsymbol{h},\boldsymbol{v}\}} \begin{bmatrix} \hat{h}_i\cdot\hat{H} & \hat{h}_i\cdot\hat{V}_i \\ \hat{v}_i\cdot\hat{H} & \hat{v}_i\cdot\hat{V}_i \end{bmatrix} = R_s^T \mathbf{S}_{\{\boldsymbol{h},\boldsymbol{v}\}} R_i. \tag{21}$$

Note that the scattering matrices are labeled with different polarization bases. The labels will be dropped hereafter in the report when doing so does not incur apparent confusion.

The polarization rotation as prescribed in Eq. (21) is equivalent to a rigid-body transformation in the 3D space. The original coordinate system is now rotated to a new system in which the X- and Y-axes can be defined as the directions of $\hat{k}_i \times \hat{k}_s$ and $\hat{k}_s + \hat{k}_i$, respectively. The bisector line between $-\hat{k}_i$ and $\hat{k}_s$,

$$\hat{b} = (\hat{k}_s - \hat{k}_i)/|\hat{k}_s - \hat{k}_i|, \tag{22}$$

will act as the Z-axis. Let $\eta = \beta/2$, and we have $\hat{b} = (\hat{k}_s - \hat{k}_i)/2\cos\eta$. Then, the incident wave comes from $(\eta, -\pi/2)$ and the scattered wave propagates toward $(\eta, \pi/2)$. The full transformation can be executed in two steps: first rotated around the axis $\hat{Z} \times \hat{b}$ by an angle $\cos^{-1}(\hat{Z}\cdot\hat{b})$, and then rotated around $\hat{Z}$ to align $-\hat{H}$ with X. The target orientation will be updated correctly using this full transformation operation.

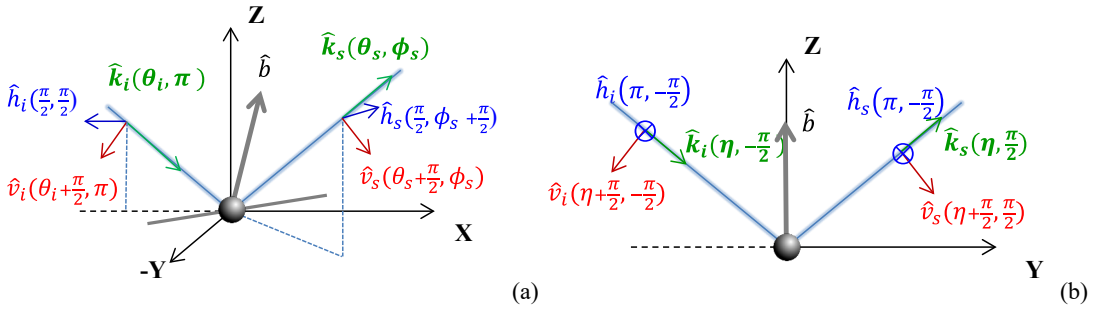

Fig. 2—Beam geometry and polarization reference system: (a) the native observation system; (b) the standard bistatic reference system with the bisector vector $\hat{b}$ defined as Z-axis. The bistatic angle equals to 2η.

2.3 The Characteristic Properties

The close association between the polarimetric observations and the adopted polarization bases can be problematic. Instead, we prefer to base the polarimetric analysis on the characteristic scattering elements that are tied more closely to the scattering process.

In order to derive the characteristic scattering variables, first we diagonalize the bistatic scattering matrix using the singular value decomposition (SVD) following

$$\mathbf{S} = \mathbf{U}\,\mathbf{D}\,\mathbf{V}^H = \mathbf{U}\begin{bmatrix} s_a & 0 \\ 0 & s_b \end{bmatrix}\mathbf{V}^H, \tag{23}$$

where the superscript "H" denotes conjugate transpose and s_a and s_b represent a pair of characteristic scattering coefficients. Both U and V are unitary matrices, expressing the polarization basis transformation from the observation bases to the characteristic bases. Therefore, it features a pair of complex polarization ratios in

$$\chi_s = \frac{U(2,1)}{U(1,1)}, \text{ and} \tag{24}$$

$$\chi_i = \frac{V(2,1)}{V(1,1)}. \tag{25}$$

The exact form of **U** and **V** is not unique. We may choose a specific form, defined as a product of the polarization rotation factor and the helical factor, such as

$$\mathbf{U} = \begin{bmatrix} \cos\tau_s & -\sin\tau_s \\ \sin\tau_s & \cos\tau_s \end{bmatrix} \begin{bmatrix} \cos\epsilon_s & j\sin\epsilon_s \\ j\sin\epsilon_s & \cos\epsilon_s \end{bmatrix}, \tag{26}$$

$$\mathbf{V} = \begin{bmatrix} \cos\tau_i & -\sin\tau_i \\ \sin\tau_i & \cos\tau_i \end{bmatrix} \begin{bmatrix} \cos\epsilon_i & j\sin\epsilon_i \\ j\sin\epsilon_i & \cos\epsilon_i \end{bmatrix}. \tag{27}$$

Both of them have a real-valued determinant. This additional constraint ensures a unique determination of the complex-valued diagonal terms, s_a and s_b.

Angles τ and ϵ represent the orientation and ellipticity of the characteristic polarization state [5, 9, 17]. Using the linear H and V polarizations in the sensing system, the former is related to the polarization basis and the target orientation, whereas the latter measures the helicity in the scattering process. They are related to the complex polarization ratio χ as follows:

$$\tan 2\tau = \frac{2\Re(\chi)}{1-|\chi|^2}, \tag{28}$$

$$\sin 2\epsilon = \frac{2\Im(\chi)}{1+|\chi|^2}, \tag{29}$$

$$\chi = \frac{\tan\tau + j\tan\epsilon}{1 - j\tan\tau\tan\epsilon}. \tag{30}$$

Note that having a standard reference system as defined in Eqs. (17)–(19) facilitates a consistent interpretation and comparison on the τ angles.

Furthermore, we define the following ratio and phase shift to represent the characteristic scattering properties:

$$\Gamma = \frac{|s_a|^2}{|s_b|^2}, \tag{31}$$

$$\nu = \angle s_a s_b^*. \tag{32}$$

The ratio is a measure of scatter polarizability and the phase shift, usually referred to as the skip angle, can potentially reveal the wave-bouncing property.

However, the polarimetric scattering response may present an incoherent process, for example, due to surface roughness. In this case, it requires an expression of the covariance matrix to completely capture the scattering information through

$$\mathbf{\Sigma} = \left\langle \underline{\boldsymbol{S}}\, \underline{\boldsymbol{S}}^H \right\rangle, \tag{33}$$

where $\underline{\boldsymbol{S}}$ is in a vectorized form, defined as $\underline{\boldsymbol{S}} = [s_{HH} \;\; s_{VH} \;\; s_{HV} \;\; s_{VV}]^T$. This covariance matrix can be decomposed into 4 uncorrelated scattering components in terms of its eigenvectors:

$$\mathbf{\Sigma} = \sum_{i=1}^{4} \lambda_i \underline{\boldsymbol{S}}_i \underline{\boldsymbol{S}}_i^H. \tag{34}$$

Each of the eigen scattering components can be diagonalized using Eq. (23) for its characteristic polarization states as well as its characteristic scattering properties. In this manner, λ, Γ, and ν are all independent of the polarization bases.

3 BISTATIC SCATTERING MODELS

The first part of this work is to derive the bistatic scattering response from several basic targets of arbitrary orientation. With the derived bistatic scattering matrices, we proceed to characterize the key scattering signatures. The incident wave is assumed incoming from the direction (θ_i, π), and the scattering wave is assumed received at the direction (θ_s, ϕ_s). Such observation system is illustrated in Fig. 2(a). For reference, the associated native polarization states in the observation system are listed as follows:

$$\hat{h}_i = [0 \quad 1 \quad 0]^T \tag{35}$$

$$\hat{v}_i = [-\cos\theta_i \quad 0 \quad -\sin\theta_i]^T \tag{36}$$

$$\hat{h}_s = [-\sin\phi_s \quad \cos\phi_s \quad 0]^T \tag{37}$$

$$\hat{v}_s = [\cos\theta_s\cos\phi_s \quad \cos\theta_s\sin\phi_s \quad -\sin\theta_s]^T \tag{38}$$

3.1 Rayleigh Dielectric Sphere

The simplest case is the isotropic scattering, where the target orientation is irrelevant. A sphere is completely symmetric in every direction. If its size is small enough, Rayleigh scattering applies and its scattering is isotropic.

Assume the sphere center is located at the origin. The incited dipole depends on the incident polarization state. For an incident field $\vec{p}_i$, the scattered field in the far field received in the direction of $\hat{k}_s$ is known as $(\hat{k}_s \times \vec{p}_i) \times \hat{k}_s = \vec{p}_i - (\vec{p}_i \cdot \hat{k}_s)\hat{k}_s$. The bistatic scattering matrix can be derived from

$$\mathbf{S} = \begin{bmatrix} [(\hat{k}_s \times \hat{h}_i) \times \hat{k}_s] \cdot \hat{h}_s & [(\hat{k}_s \times \hat{v}_i) \times \hat{k}_s] \cdot \hat{h}_s \\ [(\hat{k}_s \times \hat{h}_i) \times \hat{k}_s] \cdot \hat{v}_s & [(\hat{k}_s \times \hat{v}_i) \times \hat{k}_s] \cdot \hat{v}_s \end{bmatrix} = \begin{bmatrix} \hat{h}_i \cdot \hat{h}_s & \hat{v}_i \cdot \hat{h}_s \\ \hat{h}_i \cdot \hat{v}_s & \hat{v}_i \cdot \hat{v}_s \end{bmatrix}. \tag{39}$$

It clearly shows that the scattering response is completely related to the system polarization differences resulted from the sensing geometry.

Using the native polarization states in the observation system, we get

$$\mathbf{S} = \begin{bmatrix} \cos\phi_s & \cos\theta_i\sin\phi_s \\ \cos\theta_s\sin\phi_s & \sin\theta_i\sin\theta_s - \cos\theta_i\cos\theta_s\cos\phi_s \end{bmatrix}. \tag{40}$$

This simple case demonstrates the fundamentals described earlier. The scattering matrix is not symmetric unless $\theta_i = \theta_s$. If the incidence direction and the scattering direction are reversed, the reverse-path scattering matrix becomes

$$\mathbf{S}_{\{hv\}} = \begin{bmatrix} \cos\phi_s & -\cos\theta_s\sin\phi_s \\ -\cos\theta_i\sin\phi_s & \sin\theta_i\sin\theta_s - \cos\theta_i\cos\theta_s\cos\phi_s \end{bmatrix}, \tag{41}$$

to which the reciprocal theorem is conformed.

Applying the polarization states in the standard reference system, as shown in Fig. 2(b), leads to the scattering matrix

$$\mathbf{S}_{\{HV\}} = \begin{bmatrix} 1 & 0 \\ 0 & -\cos\beta \end{bmatrix}. \tag{42}$$

It is straightforward to verify that $\mathbf{S}_{\{HV\}} = \mathbf{R}_s^T(\alpha_s)\mathbf{S}_{\{hv\}}\mathbf{R}_i(\alpha_i)$. Therefore, the diagonal scattering matrix in Eq. (42) shows the characteristic scattering, attained using the polarization rotation angles associated with the change of the reference systems.

Figure 3 illustrates the polarimetric scattering variation as the scattering direction changes. The incidence is fixed at $\theta_i = 35°$, whereas the reception direction varies in the upper hemisphere. The polarization rotation angles clearly show the systematic changes due to the sensing geometry (see Fig. 3(a, b)). They can be verified in closed form as

$$\tan\alpha_i = \frac{\sin\theta_s \sin\phi_s}{\sin\theta_i\cos\theta_s + \cos\theta_i \sin\theta_s \cos\phi_s} \tag{43}$$

$$\tan\alpha_s = \frac{\sin\theta_i \sin\phi_s}{\cos\theta_i\sin\theta_s + \sin\theta_i \cos\theta_s \cos\phi_s} \tag{44}$$

The bistatic angle modulates the characteristic scattering ratio and the skip angles (see Fig.3(c,d)). Particular caution must be exercised in using the skip angle to judge the bouncing numbers. The bistatic angle alone can change the skip angle from 0° to 180°, which is related to the bistatic angle.

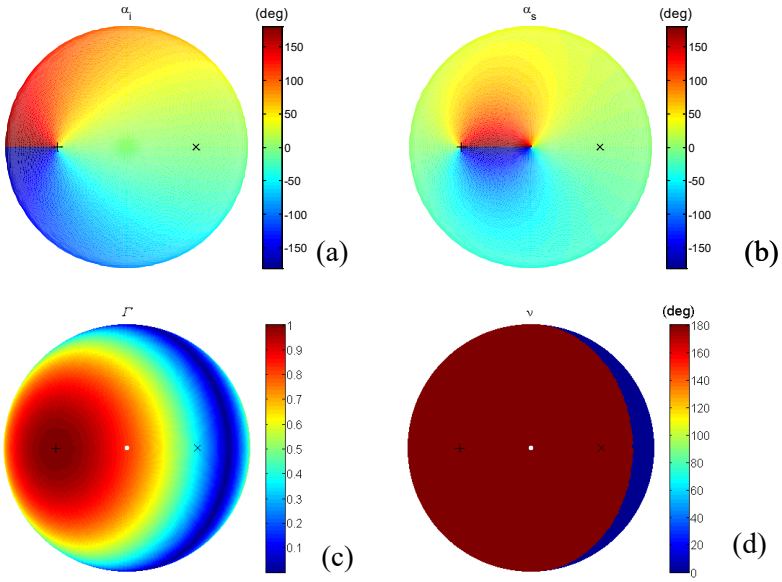

Fig. 3—The characteristic polarization parameters of dielectric sphere scattering at varying receiving directions: (a) incidence side polarization rotation; (b) scattering side polarization rotation; (c) inter-polarization scattering ratio; (d) the skip angle. The symbol "+" marks for the fixed incidence direction and the symbol "x" marks for the specular scattering direction. The scattering wave is received at varying direction in the upper hemisphere, with the radius measuring the zenith angle and the concentric locations measuring the azimuth angle.

3.2 Specular Scattering

Specular scattering used to draw the most common interest in the bistatic sensing configuration. It is a special case in which the forward scattering direction is fixed to the direction at

$$\hat{k}_s = \hat{k}_i - 2\left(\hat{k}_i \cdot \hat{n}\right)\hat{n} = \hat{k}_i + 2\cos\eta\,\hat{n}, \tag{45}$$

where $\hat{n}$ defines the normal to the illustrated surface of the target. When the scattering is known resulted from specular scattering, the surface normal needs to be the bisector vector. In other words, the surface normal vector points to Z under the standard reference frame.

Then, the scattering matrix is diagonal, following the well-known relation of

$$\mathbf{S}_0 = \begin{bmatrix} \frac{\cos\eta - \sqrt{\varepsilon_r - \sin^2\eta}}{\cos\eta + \sqrt{\varepsilon_r - \sin^2\eta}} & 0 \\ 0 & \frac{\varepsilon_r\cos\eta - \sqrt{\varepsilon_r - \sin^2\eta}}{\varepsilon_r\cos\eta + \sqrt{\varepsilon_r - \sin^2\eta}} \end{bmatrix}, \tag{46}$$

where ε_r is the relative permittivity of the target. In reality, the surface normal, either of sloped terrain or of structure facets, can point to any direction. Then, the aforementioned polarization rotation still applies and the observed specular scatter response is not necessarily diagonal. This is also a simple bistatic scattering case: although the target orientation matters, its normal direction is uniquely determined from the sensing geometry. Only the relative permittivity is the parameter to be estimated.

Figure 4 illustrates the polarimetric scattering variation off a specular surface as its orientation changes in the upper hemisphere. The incidence is fixed at $\theta_i = 35°$ and we assume the receiver is always located at the right direction. Figure4(a) and (b) show the polarization rotation angles resolved from the characteristic polarization states. The surface orientation with beam blockage is masked out in the plots. Figure 4(c) and (d) show the characteristic scattering ratio and the skip angles. A dip is also present in the characteristic ratio, and the skip angle also changes. However, this is associated with the Brewster angle with dependence on the relative permittivity, which is clearly delineated in Fig. 5. As ε_r increases, the incidence where the change occurs shifts to larger angles. The characteristic ratio does not go to zero because the relative permittivity also has an imaginary part.

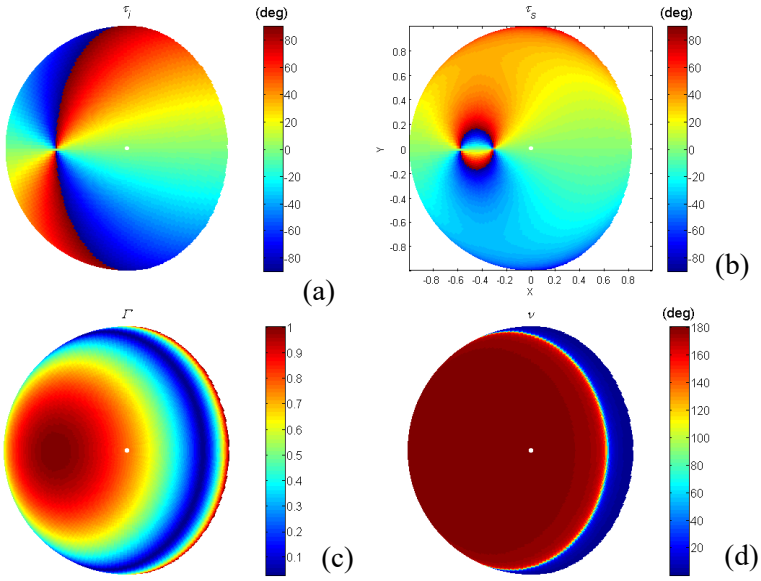

Fig. 4—Same as Fig.3 except for the characteristic polarization parameters of specular scattering. The positions in the plots indicate the surface normal direction, effectively varying the receiving directions.

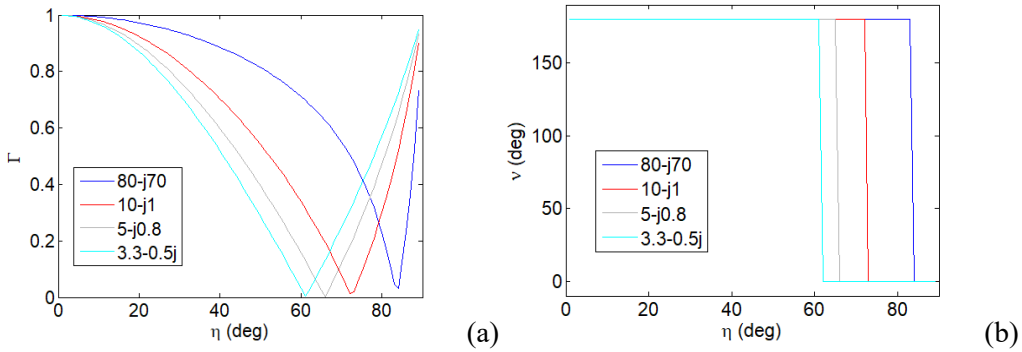

Fig. 5—The dependence of (a) the scattering ratio and (b) the skip angle on the bistatic angle and the relative permittivity. The skip angle can change at a bistatic setting related to the permittivity.

3.3 Double-Bounce Scattering

Double bounce represents an important scattering mechanism in polarimetric SAR imagery analysis. It comes from a target with two facets forming a right dihedral angle. An identified double bounce signature indicates the presence of urban buildups or other man-made structures. The wave path will involve two specular reflections off the dihedral facets. Accordingly, to receive double-bounce scattering, the sensing geometry also needs to satisfy a special condition.

Let a dihedral reflector is formed by a vertical facet with normal $\hat{n}_w$ and a horizontal facet with normal $\hat{n}_g$, jointed at the seam line along direction $\hat{l}_j$. Assume $\hat{l}_j = \hat{n}_g \times \hat{n}_w$. As shown in Fig. 6, after bouncing twice off the vertical face and then off the horizontal face, the reflected beam would point to the direction:

$$\begin{aligned}\hat{k}_s &= \hat{k}_i - 2(\hat{k}_i \cdot \hat{n}_w)\hat{n}_w - 2[(\hat{k}_i - 2(\hat{k}_i \cdot \hat{n}_w)\hat{n}_w) \cdot \hat{n}_g]\hat{n}_g \\ &= \hat{k}_i - 2(\hat{k}_i \cdot \hat{n}_w)\hat{n}_w - 2(\hat{k}_i \cdot \hat{n}_g)\hat{n}_g. \end{aligned} \quad (47)$$

It is apparent that the bouncing order for the propagation path does not alter the scattering direction. The bisector vector can be then evaluated from

$$\hat{b} = \frac{1}{\sqrt{2(1+\cos\beta)}}[-2(\hat{k}_i \cdot \hat{n}_w)\hat{n}_w - 2(\hat{k}_i \cdot \hat{n}_g)\hat{n}_g] = \frac{1}{\sqrt{\cos^2\eta_w + \cos^2\eta_g}}[\cos\eta_w\,\hat{n}_w + \cos\eta_g\,\hat{n}_g], \quad (48)$$

where η stands for the local beam angles with respect to the surface normal vectors. According to Eq. (48), $\hat{b} \perp \hat{l}_j$. In addition, note that

$$\hat{k}_i \times \hat{k}_s = 2\cos\eta_w\,(\hat{k}_i \times \hat{n}_w) + 2\cos\eta_g\,(\hat{k}_i \times \hat{n}_g). \quad (49)$$

We can find it is also perpendicular to $\hat{l}_j$. Therefore, the seam line is contained on the bistatic plane, forming a specular geometry. If we rotate the system to the standard reference frame, the seam line would align with the Y-axis.

In the standard reference frame, let the elevation angle of the dihedral reflector be θ such that $\hat{n}_w = [\cos\theta \quad 0 \quad \sin\theta]^T$ and $\hat{n}_g = [-\sin\theta \quad 0 \quad \cos\theta]^T$. In addition, its two faces may feature different permittivity, noted as ε_w and ε_g.

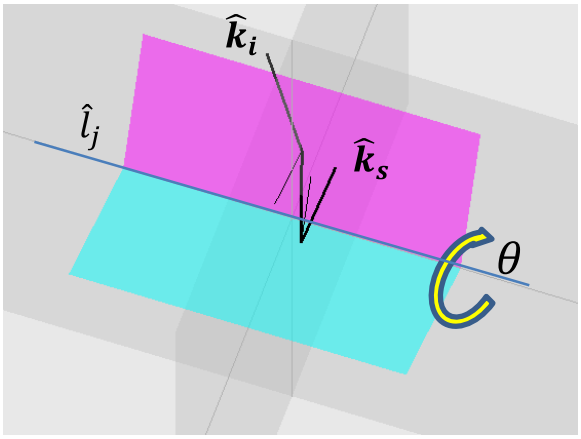

Fig. 6—Diagram of a dihedral reflector with one of the two double-bounce scattering paths

For the first path along which the wave first bounces off the vertical face, the specular scattering described in the previous section applies. Transforming the incident polarization states to the $\hat{n}_w$-based local system requires the following rotation matrix:

$$\mathbf{R}_i = \begin{bmatrix} \sin\theta\sin\eta & \cos\theta \\ -\cos\theta & \sin\theta\sin\eta \end{bmatrix}. \quad (50)$$

The outgoing wave proceeds along the direction $\hat{k}_r = \hat{k}_i - 2(\hat{k}_i \cdot \hat{n}_w)\hat{n}_w$ toward the horizontal face. Its polarization states defined in the $\hat{n}_w$-based local system needs again to be transformed onto the $\hat{n}_g$-based local system, which can be found following

$$\mathbf{R}_r = \begin{bmatrix} \sin\theta\cos\theta\cos^2\eta & \sin\eta \\ -\sin\eta & \sin\theta\cos\theta\cos^2\eta \end{bmatrix}. \tag{51}$$

The reflected wave after the second bounce propagates along $\hat{k}_s$, and its polarization states can be transformed back to the observation basis using another rotation matrix,

$$\mathbf{R}_s = \begin{bmatrix} \cos\theta\sin\eta & -\sin\theta \\ \sin\theta & \cos\theta\sin\eta \end{bmatrix}. \tag{52}$$

The scattering matrix for this path can be written as

$$\mathbf{S}_1 = \mathbf{R}_s\mathbf{S}_0(\varepsilon_g, \eta_g)\mathbf{R}_r\mathbf{S}_0(\varepsilon_w, \eta_w)\mathbf{R}_i^T, \tag{53}$$

where $\mathbf{S}_0$ is a diagonal matrix as defined in Eq. (46).

There exists another path for which the wave first bounces off the ground face followed by the second bounce off the vertical surface. Following the same polarization manipulation, we can derive its associated scattering matrix as

$$\mathbf{S}_2 = \mathbf{R}_i\mathbf{S}_0(\varepsilon_w, \eta_w)\mathbf{R}_r^T\mathbf{S}_0(\varepsilon_g, \eta_g)\mathbf{R}_s^T. \tag{54}$$

Together, the double-bounce scattering from a dihedral can be described as

$$\mathbf{S} = \mathbf{S}_1 + \mathbf{S}_2 = \mathbf{R}_s\mathbf{S}_0(\varepsilon_g, \eta_g)\mathbf{R}_r\mathbf{S}_0(\varepsilon_w, \eta_w)\mathbf{R}_i^T + \mathbf{R}_i\mathbf{S}_0(\varepsilon_w, \eta_w)\mathbf{R}_r^T\mathbf{S}_0(\varepsilon_g, \eta_g)\mathbf{R}_s^T, \tag{55}$$

which is a symmetric matrix. If both dihedral faces are perfect conductor, $\mathbf{S}_0 = diag(-1,1)$, and we find $\mathbf{S} = diag(1,1)$, which is the same as the monostatic dihedral scattering matrix in the FSA convention. Other than that, the bistatic double-bounce-scattering signature (Fig. 7) is very different from its monostatic one.

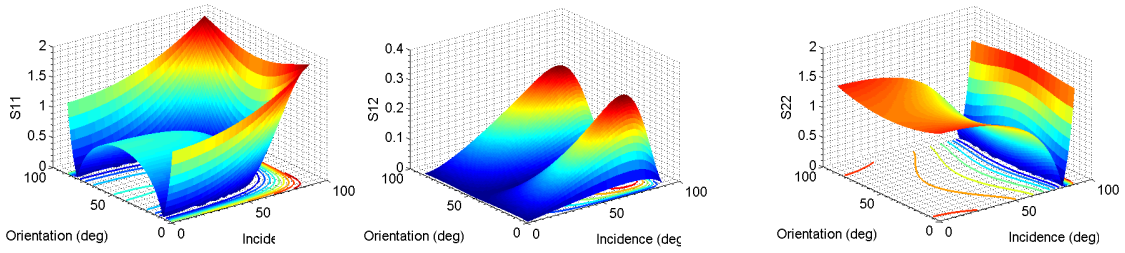

Fig. 7—The bistatic double-bounce scattering signature of a dihedral corner reflector at changing incidence angle (η) and dihedral orientation angle (θ)

3.4 Surface Scattering

When the surface is rough, its bistatic scattering response can be observed in a general sensing geometry. Modeling the surface scattering of various roughness is critical to remote sensing and a longstanding research thrust. In general, with increased roughness, we start to see scattering responses in nonspecular directions. If the roughness is small, the scattered return is primarily coherent and we can apply the first-order small perturbation method (SPM) [18, 19]. When the roughness is large, scattering becomes diffusive and the scattered return is incoherent such that second-order statistics is needed to describe the scattering property [20].

Given a horizontal rough surface under wave illustration from direction $(\theta_i, -\pi)$, as illustrated in Fig. 2(a), the bistatic polarimetric scattering at direction (θ_s, ϕ_s) can be expressed according to SPM as [21]

$$\mathbf{S}_0 = \begin{bmatrix} \frac{\cos\phi_s}{\left(\cos\theta_i+\sqrt{\varepsilon_r-\sin^2\theta_i}\right)\left(\cos\theta_s+\sqrt{\varepsilon_r-\sin^2\theta_s}\right)} & \frac{\sin\phi_s\sqrt{\varepsilon_r-\sin^2\theta_i}}{\left(\varepsilon_r\cos\theta_i+\sqrt{\varepsilon_r-\sin^2\theta_i}\right)\left(\cos\theta_s+\sqrt{\varepsilon_r-\sin^2\theta_s}\right)} \\ \frac{\sin\phi_s\sqrt{\varepsilon_r-\sin^2\theta_s}}{\left(\cos\theta_i+\sqrt{\varepsilon_r-\sin^2\theta_i}\right)\left(\varepsilon_r\cos\theta_s+\sqrt{\varepsilon_r-\sin^2\theta_s}\right)} & \frac{\varepsilon_r\sin\theta_i\sin\theta_s-\cos\phi_s\sqrt{\varepsilon_r-\sin^2\theta_i}\sqrt{\varepsilon_r-\sin^2\theta_s}}{\left(\varepsilon_r\cos\theta_i+\sqrt{\varepsilon_r-\sin^2\theta_i}\right)\left(\varepsilon_r\cos\theta_s+\sqrt{\varepsilon_r-\sin^2\theta_s}\right)} \end{bmatrix}. \tag{56}$$

Backscattering occurs at $\phi_s = -\pi$ and forward specular scattering occurs at $\phi_s = 0$, both having symmetric scattering matrices. In other general scenarios, the surface normal is off the bistatic plane and the scattering matrix is not symmetric. Furthermore, in reality, we often need to deal with sloped terrain, where the surface normal points to nonvertical directions.

For a surface with its normal vector $\hat{n}$ pointing to direction (θ, ϕ), in Eq. (56), we need use the local beam angles relative to the surface, which can be converted from their native beam variables through

$$\theta_i = \cos^{-1}\left(-\hat{k}_i \cdot \hat{n}\right), \tag{57}$$

$$\theta_s = \cos^{-1}\left(\hat{k}_s \cdot \hat{n}\right), \tag{58}$$

$$\phi_s = \cos^{-1}\left[\left(\cos\theta_i\cos\theta_s + \hat{k}_i \cdot \hat{k}_s\right)/\left(\sin\theta_i\sin\theta_i\right)\right]. \tag{59}$$

We still want to use the standard reference system in order to establish a common basis for polarimetric analysis and characterization. In this system, the beam angles are first computed from Eqs. (57)–(59). The ensuing scattering matrix is not diagonal as evident from Eq. (59) with ϕ_s of general settings. Next, the polarization states valid in Eq. (56) need to be rotated to the reference frame using

$$\mathbf{R}_{i0} = \frac{1}{\sin\theta_i}\begin{bmatrix} \sin\eta\cos\theta + \cos\eta\sin\theta\sin\phi & \sin\theta\cos\phi \\ -\sin\theta\cos\phi & \sin\eta\cos\theta + \cos\eta\sin\theta\sin\phi \end{bmatrix}, \tag{60}$$

$$\mathbf{R}_{s0} = \frac{1}{\sin\theta_s}\begin{bmatrix} \sin\eta\cos\theta - \cos\eta\sin\theta\sin\phi & \sin\theta\cos\phi \\ -\sin\theta\cos\phi & \sin\eta\cos\theta - \cos\eta\sin\theta\sin\phi \end{bmatrix}. \tag{61}$$

The general scattering matrix for an oriented surface is then evaluated as

$$\mathbf{S}(\theta, \phi; \eta) = \mathbf{R}_{s0}\mathbf{S}_0(\theta_i, \theta_s, \phi_s)\mathbf{R}_{i0}^T. \tag{62}$$

Figure 8 shows the bistatic polarimetric scattering variation associated with a horizontal, slightly rough surface. The incidence is fixed at $\theta_i = 35°$, whereas the reception direction varies in the upper hemisphere, and the permittivity is set as $\varepsilon_r = 9.2 - j0.5$. The observations have been firstly transformed to the standard reference frame. The polarization orientation angles are different between the incidence side and the receiving side. Abrupt changes occur when the incidence plane and the scattering plane are nearly aligned together on the backward side. Without the transformation, the polarization orientation angles will be

dominated by the system polarization difference. The characteristic polarizations now have a nonzero ellipticity, likely indicating a small helical component due to target asymmetry with respect to the bistatic plane. When the surface normal is contained in the bistatic plane, the polarization ellipticity is zero and the polarizability can reach the lowest (with Γ approaching 1). The location of the lowest polarizability depends on both the surface orientation and the surface permittivity. The skip angle indicates out-phase characteristic components everywhere.

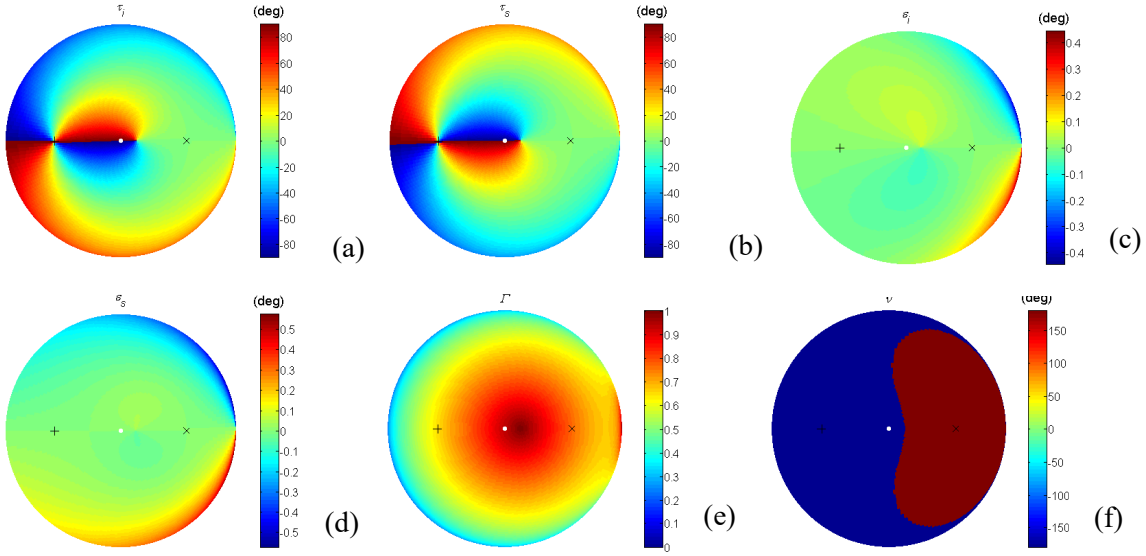

Fig. 8—Same as Fig.3 except for the characteristic polarization parameters of a slightly rough, horizontal surface scattering at varying receiving directions. Panels (c) and (d) show the small but nonzero ellipticity angles.

3.5 Volume Scattering

Radar scattering from vegetated land covers is usually modeled as a random volume, with each individual scatterer occupying a random position inside the resolution cell. Because of this randomness, the scattering response is neither coherent nor completely polarized and its characterization needs to rely on second-order statistics, such as using covariance matrices. Furthermore, the scatterers, including leaves and twigs, also have random orientation, which severely changes the polarimetric field from one scatterer to another [22–24].

We use a spheroid to model both the shape and the orientation of a general vegetation scatterer [25]. It defines an elliptical shape rotated vs. a symmetric axis, illustrated in Fig.9. A prolate spheroid results from rotating around the major axis and an oblate spheroid results from rotating around the minor axis. The rotation axis is oriented in the direction of (θ, ϕ). The elliptical shape induces different polarizabilities between along and perpendicular to the symmetric axis, noted as α_z and α. Then, the elementary scattering coefficient can be derived as

$$s_{uv} = \alpha_z \langle t_z, u \rangle \langle t_z, v \rangle + \alpha \langle t_x, u \rangle \langle t_x, v \rangle + \alpha \langle t_y, u \rangle \langle t_y, v \rangle, \tag{63}$$

where u and v are the receiving and incident polarization respectively, and t_x, t_y and t_z represent the reference axes for the spheroid body with t_z being the rotation axis.

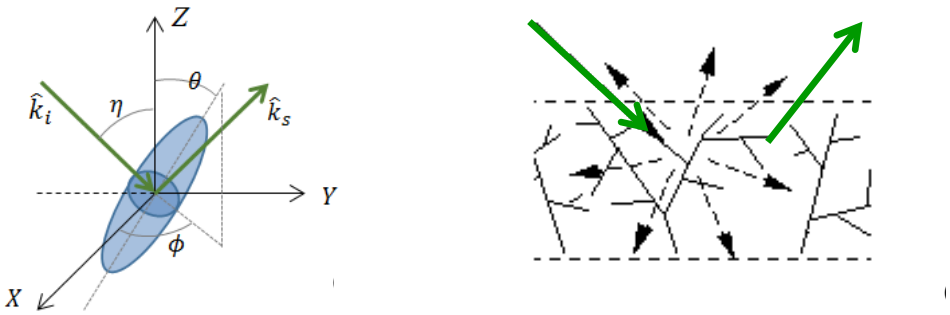

Fig. 9—(a) A spheroid with the symmetric axis oriented at (θ, ϕ); (b) a random volume of vegetation scatterers

Under the standard reference system, the bistatic scattering from an oriented spheroid can be expressed in the matrix

$$\mathbf{S} = \alpha \mathbf{S}_{sphere} + (\alpha_z - \alpha) \times \begin{bmatrix} \sin\theta\cos\phi \\ \cos\theta\sin\eta - \sin\theta\sin\phi\cos\eta \end{bmatrix} [\sin\theta\cos\phi \quad \cos\theta\sin\eta + \sin\theta\sin\phi\cos\eta]. \tag{64}$$

As shown, it is attributed to two parts, one from an ideal sphere and another from an oriented dipole. Overall, it is a function of the bistatic angle (through η), the scatter shape (through α_z and α), and the scatter orientation (through θ and ϕ). The covariance matrix can be evaluated as

$$\mathbf{\Sigma} = \int \langle \underline{\boldsymbol{S}}\, \underline{\boldsymbol{S}}^H \rangle f(\theta, \phi) \sin\theta \, d\theta d\phi, \tag{65}$$

where $\boldsymbol{S}$ is the vectorized form of $\mathbf{S}$, and f stands for the probability density function (PDF) of the orientation distribution.

It is unrealistic to cover all the possible physical vegetation characteristics in Eq. (65) considering the diversity in natural land covers. In practice, we apply some reasonable approximation and generalization to capture the main variation features. Firstly, we assume the shape variation and the orientation variation are mutually independent. Secondly, we assume the mean orientation for all vegetation scatterers distributed vertically. Additionally, we also commonly assume the orientation is uniformly distributed, i.e.,

$$f(\theta, \phi) = \frac{1}{4\pi}. \tag{66}$$

Then, replacing Eqs. (64) and (66) in Eq. (65) leads to the following covariance matrix:

$$\begin{bmatrix} \frac{8|\alpha|^2+3|\alpha_z|^2+4Re(\alpha\alpha_z^*)}{15} & 0 & 0 & -\cos\beta\frac{6|\alpha|^2+|\alpha_z|^2+8Re(\alpha\alpha_z^*)}{15} \\ 0 & \frac{|\alpha|^2+|\alpha_z|^2-2Re(\alpha\alpha_z^*)}{15} & -\cos\beta\frac{|\alpha|^2+|\alpha_z|^2-2Re(\alpha\alpha_z^*)}{15} & 0 \\ 0 & -\cos\beta\frac{|\alpha|^2+|\alpha_z|^2-2Re(\alpha\alpha_z^*)}{15} & \frac{|\alpha|^2+|\alpha_z|^2-2Re(\alpha\alpha_z^*)}{15} & 0 \\ -\cos\beta\frac{6|\alpha|^2+|\alpha_z|^2+8Re(\alpha\alpha_z^*)}{15} & 0 & 0 & \frac{|\alpha|^2+|\alpha_z|^2-2Re(\alpha\alpha_z^*)}{15} + \cos^2\beta\frac{7|\alpha|^2+2|\alpha_z|^2+6Re(\alpha\alpha_z^*)}{15} \end{bmatrix} \tag{67}$$

Two limiting cases are of particular interest. At low frequency, the scattering response from twigs likely dominates. The scatter shape can be treated as randomly oriented needles, i.e., $\alpha = 0$. This is also reasonable for coniferous canopy. In this case, the covariance matrix in Eq. (67) reduces to:

$$\frac{1}{15}\begin{bmatrix} 3 & 0 & 0 & -\cos\beta \\ 0 & 1 & -\cos\beta & 0 \\ 0 & -\cos\beta & 1 & 0 \\ -\cos\beta & 0 & 0 & 1+2\cos^2\beta \end{bmatrix}. \tag{68}$$

Setting $\beta = 0$, we will get the widely used monostatic random volume scattering covariance matrix. At high frequency, the scattering response from leaves likely dominate. In this case, for broadleaf canopy we can approximate the scatter shape as randomly oriented disks and the covariance matrix in Eq. (67) reduces to

$$\frac{1}{15}\begin{bmatrix} 8 & 0 & 0 & -6\cos\beta \\ 0 & 1 & -\cos\beta & 0 \\ 0 & -\cos\beta & 1 & 0 \\ -6\cos\beta & 0 & 0 & 1+7\cos^2\beta \end{bmatrix} \tag{69}$$

We should note there used to be a common misconception that the random disk scattering is isotropic like spheres. Comparing Eq. (69) to Eq. (42) indicates they in fact are different.

The random disk scattering features a lower cross-polar channel and a higher interchannel correlation coefficient. Additionally, the bistatic angle will modulate the polarimetric difference between random disk volume and random needle volume. Figure10 shows the correlation coefficient between S_{HH} and S_{VV} at various bistatic angles. The difference is the largest at the backscattering direction and the lowest at the forward-scattering direction. Over a wide range of bistatic settings (up to 70°), the difference retains its significance and this variation can be useful to distinguish different vegetation scatter types.

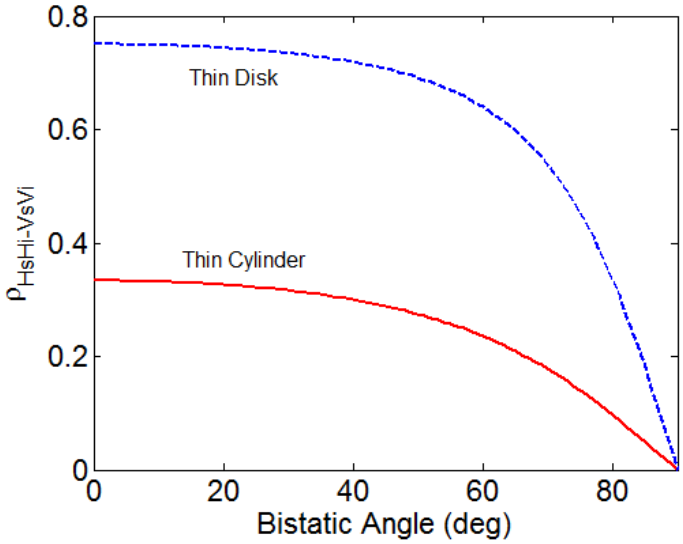

Fig. 10—The varying difference between the inter-channel correlation coefficients of random disk scatter and random needle scatter at different bistatic angles

4 POTENTIAL APPLICATIONS

The second part of this work is to explore the utility of the polarimetric bistatic SAR imagery. The bistatic scattering models clearly demonstrate that the scattering response in any single polarization channel is heavily hinged on the bistatic geometry. Assuming we collect the full polarimetric set with four degrees of freedom (as compared against the three degrees of freedom in the monostatic case), we want to address what added values we can expect to gain from bistatic SAR observations.

4.1 Scatter Parameter Estimation

Having the bistatic scattering models developed, the following question is whether the scatter parameters can be uniquely and reliably determined from the full polarimetric dataset. As the first step, we assume we know the specific scattering mechanism; based on that, we investigate the estimation of the scatter parameters involved in those scattering models. The key focus is to evaluate the capability and the limitation of bistatic observations as against monostatic observations.

4.1.1 Specular Scattering Parameters

Recall Eq. (46). Since η can be determined from the sensing geometry, ε_r is the only parameter to estimate and the inversion can be done through the following trivial process.

We define the ratio VV/HH as K and define $t = \sqrt{\varepsilon_r - \sin^2\eta}$. Then,

$$K = \frac{(t^2+\sin^2\eta)\cos\eta - t}{(t^2+\sin^2\eta)\cos\eta + t} \cdot \frac{\cos\eta + t}{\cos\eta - t} = \frac{\sin^2\eta - t\cos\eta}{\sin^2\eta + t\cos\eta}. \tag{70}$$

This leads to the unique solution:

$$t = \frac{(1-K)\sin^2\eta}{(1+K)\cos\eta}, \tag{71}$$

provided that $K \neq -1$ and $\eta \neq \pm 90°$.

4.1.2 Dihedral Scattering Parameters

Similarly to the monostatic case, the bistatic dihedral scattering has restricted sensing geometry. However, a dihedral scatter can be rotated by an angle around the joint line of its two perpendicular facets. In contrast, to receive monostatic dihedral scattering, the dihedral can be additionally rotated around the incident beam, which is well known incurring a polarization rotation angle.

Because the bistatic scattering matrix is symmetric, we only have four real-valued equations to use after discarding the absolute scale and phase factor. The unknown parameters to solve generally include two complex-valued permittivity and the rotation angle θ. The inversion system will be underdetermined.

If the dihedral rotation angle can be determined a priori, it may be possible to solve the pair of complex-valued permittivity using nonlinear optimization. Figure 11 presents a test case in which $\varepsilon_w = 40 - j1.0$ and $\varepsilon_g = 12 - j0.3$. It shows that the nonlinear solution is not always reliable, especially at grazing incidence directions. An analysis on the solution space also reveals that the nonlinearity is very high with high sensitivity to the assumed dihedral rotation angle.

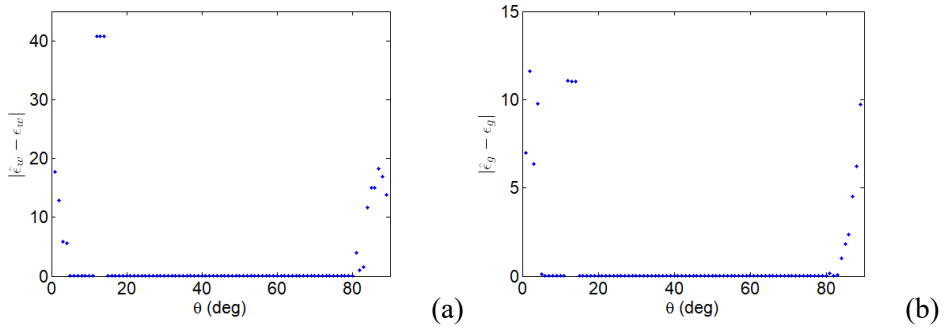

Fig. 11—The errors on the estimated permittivity, different between the two dihedral facets, under known rotation angles

If the permittivity is same between the two facets, such as of concrete corners in an urban structure, it may be possible to solve the permittivity and the dihedral rotation angle together. We still need to exercise enough caution to avoid the local optima, for example, by starting from different initial points. Figure12 presents a similar test case in which $\varepsilon_w = \varepsilon_g = 40 - j1.0$. The result implicates that the additional polarimetric channel acquired from bistatic geometries can help determine the complete dihedral physical parameters.

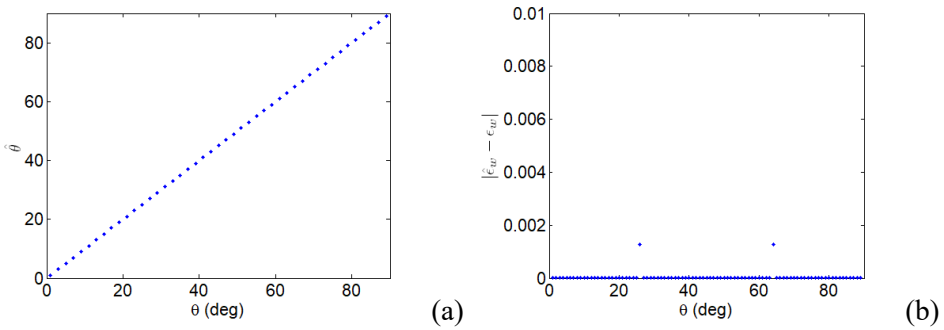

Fig. 12—The errors on the estimated rotation angle (a) and on the estimated permittivity, shared between the two dihedral facets (b)

4.1.3 Surface Scattering Parameters

For a slightly rough surface, our interest is to retrieve the surface orientation and the surface permittivity based on the SPM scattering model. Orientation is a critical piece of information for us to derive terrain slopes and topography but also to make polarimetric corrections on the observed datasets [26–31]. Orientation and permittivity are entangled in the scattering response. Together, there are four unknown variables to determine, including the pair of orientation angles and a complex-valued permittivity. With normalization on the bistatic scattering matrix, we will have six real-valued equations available. It appears feasible to estimate all the parameters using bistatic polarimetric data.

The estimation process that we explored include the following steps: (1) transform the polarimetric observations to the standard reference frame based on the sensing geometry; (2) compare the observations to the surface scattering model at the given bistatic angle and estimate both the permittivity and the surface orientation angles relative to the reference frame; (3) convert the estimated orientation angles back to the

native beam geometry. The orientation angles again induce high nonlinearity and multiple local optima, which may require multiple runs from different initial points. A case for a slightly rough surface oriented at ($\theta = 10°, \phi = 45°$) is simulated with $\eta = 35°$ and $\varepsilon_r = 9.2 - j0.5$. Fig.13 shows the estimation errors as the receiving direction varies. For the majority of scattering directions, the complete surface properties can be accurately estimated. However, the estimation faces difficulties at some sensing geometries, especially in the forward directions near the specular geometry. We have stated that it is trivial to estimate permittivity at the specular geometry. However, here we attempt to estimate both the permittivity and the orientation, with no prior knowledge that it is a specular situation. In addition, assuming a particular surface orientation in the simulation does not cause any loss of generality because the effective orientation angles change with the varying receiving directions.

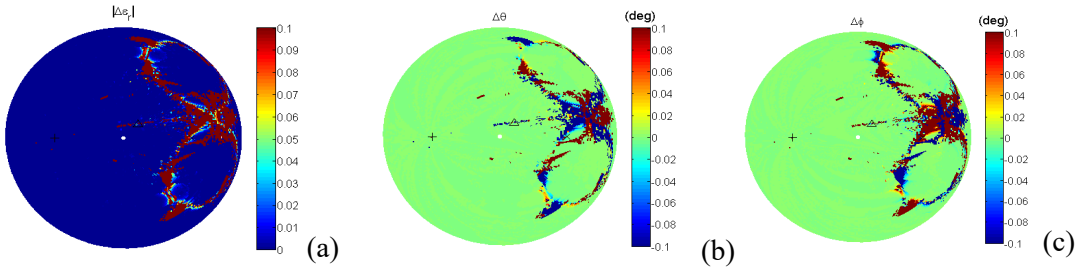

Fig 13—The errors on the estimated surface parameters using bistatic observations: (a) surface permittivity, and (b) zenith angle and (c) azimuth angle of the surface normal vector. The symbol "+" marks the incidence direction and the symbol "Δ" marks the normal vector direction. The positions in the plots indicate the scattering direction at reception.

Such complete determination of the surface properties is not possible using monostatic polarimetric observations. Monostatic SAR provides three polarimetric channels, and after normalization, we end up with four equations for the four unknown variables. Although it seems possible to solve for an inversion, the system may be mutually dependent. Particularly, the backscattering matrix can be diagonalized, resulting in only two equations, through polarization rotation (one degree of freedom). The diagonal scattering can be used to resolve ε_r only if the local incidence angle is known, whereas the polarization rotation angle cannot sufficiently map to two geometry angles of the surface normal vector.

However, we can build an augmented dataset by combining the bistatic data with their monostatic counterparts. The monostatic observation is readily available in a bistatic system. The combined dataset provides extra equations for the system inversion. We run the fused nonlinear optimization on this simulated case, and the estimation is significantly improved in robustness as shown in Fig.14. Sans a few special scattering geometries, for example when receiving at the backscattering direction, the full surface properties can be retrieved from the joint observations successfully. This potential is important since topography-induced distortion is a long-standing problem in radar remote sensing of terrain clutter.

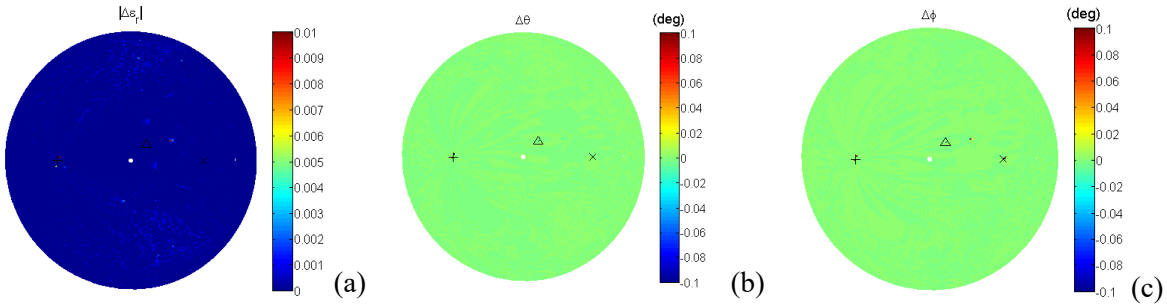

Fig 14—Same as Fig. 13, except for the estimation using joint bistatic and monostatic observations

4.2 Polarimetric Interpretation and Target Decomposition

The actual scattering in a natural scene is often complex. A man-made target is usually embedded in complex natural clutter and the clutter can contain multiple scatterers. Polarimetric target decomposition is an exploration technique to map the multichannel observations into several distinct elements, each projected to its closest scattering mechanism [5, 11].

In monostatic polarimetric analysis, target decomposition operates in two manners, either coherently in the backscattering matrices or incoherently in the covariance matrices. The former is typically performed in the Pauli basis, in which the three orthogonal components are attributed to scattering features from sphere, standard dihedral, and vegetation [32–36]. The latter is typically represented by the Freeman-Durden model-based technique, in which the backscatter covariance matrix is used to solve for three physically realizable components based on the adopted scattering models [37–39].

In bistatic polarimetric analysis, the Pauli-basis decomposition is not as useful (referring to Section 1.2.2). Moreover, the scattering responses from a standard sphere and a standard dihedral do not feature orthogonal polarimetric vectors. It is thus hindered to coherently extract distinct scattering components from the bistatic scattering matrix. Instead, we resort to the incoherent polarimetric target decomposition.

4.2.1 Eigenvector-Based Decomposition

We can operate eigenvector decomposition on the bistatic covariance matrix as outlined in Eq. (34). With the full-rank covariance matrix, we will get four coherent scattering components that are uncorrelated from each other. This likely does not resolve the true scattering components contained in the bistatic observations. However, it projects the observed polarimetric variation into orthogonal dimensions with extreme variability, a common practice in statistical analysis. The bistatic scattering model developed earlier then can be used as the basis for the interpretation of each eigen scattering component.

If an eigenvector corresponds to a diagonal matrix, the associated scattering element will have a symmetric axis aligning on the bistatic plane. We can evaluate its scattering ratio between the two copolarization channels to infer whether the scattering process comes from an isotropic scatterer-like sphere or from a slightly rough surface.

If an eigenvector corresponds to a symmetric matrix, the associated scattering element may involve a double-bounce process such as from a dihedral corner. Supplemental to this, the skip angle can be evaluated to further support this double-bounce inference.

If an eigenvector has a significant intensity but also a dominant cross-polarization channel, the associated scattering element connects with a random volume of vegetation scatterers. The randomness in the scatter orientation of vegetation is much higher than that of other scatter types, for example, a rough surface. This will distribute the scattered power more evenly to different components. Moreover, the presence of a dipole-type response from vegetation scatterers will introduce a dominant cross-polarization feature.

The rest of the eigenvectors can be associated with rough surface scattering from bare terrain. This part is, in fact, more complex because the terrain slope, the soil moisture, and the surface roughness are all entangled at a comparable level. As shown earlier, its complete characterization may require multistatic observations.

4.2.2 Model-Based Decomposition

A model-based polarimetric decomposition defines a direct approach to taking advantage of the multichannel observation for an inversion. Models of a few common scattering mechanisms are included as the "dictionary": of polarimetric responses [40, 41]. With the eigen-based decomposition, the resolved components may not match well with the true targets. The model-based decomposition addresses this issue by estimating the scattering contribution from real physical models.

The scattering response from random clutter such as vegetation will also spill over multiple eigen-based components, which can be avoided if a true matching model is included in the decomposition system. As a potential problem with the model-based decomposition, the inversion system can be underdetermined if the "dictionary" uses too many unknown parameters. For example, if we attempt to account for both random vegetation volume and random rough surface, we would not get a unique solution using the polarimetric observations [42].

We select the random volume scattering component to be estimated first. Assuming we know the vegetation canopy is dominated with needle-type scatterers, we use Eq. (68) to define its model covariance matrix $\mathbf{C}_v$. Similarly, if we know disk-type scatterers, we use Eq. (69) to define $\mathbf{C}_v$. Once we estimate its strength in the scattered return t, we can remove its contribution from the observations and get a residue covariance matrix, namely

$$\mathbf{\Sigma}_R = \mathbf{\Sigma}_{obs} - t \cdot \mathbf{C}_v. \tag{72}$$

We will assign t a value that makes the residue covariance matrix have a reduced rank, meanwhile maintaining a valid covariance matrix, for example, with nonnegative eigenvalues [43, 44]. This goal can be archived by the smallest t with which all the leading principal minors of the residue matrix equals to zero [45, 46], namely

$$t = \min\{root(|\mathbf{\Sigma}_R(1 \dots i, 1 \dots i)|) \mid i = 1, \dots, 4\}, \tag{73}$$

where $|\cdot|$ stands for determinant. This solution will keep the residue matrix positive semi-definite with zero determinant and $t \cdot \mathbf{C}_v$ will account for the random volume scattering component.

We will not allow another random scattering process in the decomposition system. After the random volume scattering is removed, we apply eigen-based decomposition on the residue covariance matrix and make inference on the scattering mechanism of each eigenvector.

During this program, we were unable to collect real bistatic PolSAR data to run target decomposition experiments. Table 1 presents a simple simulation-based target decomposition, demonstrating that the

random volume scattering severely distorts the other components, and once removed, the other components, surface scattering and double-bounce scattering can be approximately recovered based on the skip angles. The bistatic angle is set at 70° and the surface is oriented at 40° off the bisector direction and 45° off the bistatic plane. The random volume component is simulated with 10,000 uniformly oriented needle scatterers. We should exercise enough caution because the eigen-based decomposition regarding the surface component and the double-bounce component change with the bistatic geometries. However, though not precise, the decomposition results do provide critical and useful guidance for imagery interpretation and analysis.

Table 1—Polarimetric Target Decomposition Trial on Simulated Bistatic Observation (70° Bistatic Angle): Observation Model: $\mathbf{\Sigma_{obs} = 12 \cdot C_v + 5 \cdot C_s + 9 \cdot C_d}$

Variables	Component #1	Component #2	Component #3	Component #4
(Before removal of random volume scattering)				
Eigenvalue	**11.75**	**10.28**	2.67	1.30
Skip Angle (deg)	-11.0	-168.3	-1.4	-179.9
(After removal of random volume scattering)				
Eigenvalue	**9.48**	**4.65**	0.02	0.00
Skip Angle (deg)	-5.0	-172.3	-179.0	-2.6

4.2.3 Shape Adaptive Vegetation Scatter Model

In order to remove the influential random volume component, the theoretical polarimetric covariance matrix needs to be known. However, it depends on the vegetation scatter types. At short wavelengths, scattering response can be regarded as from thin disks in broadleaf forest and from needles in coniferous forest. We can use the difference between their polarimetric signatures, for example, those shown in Fig. 10, to develop an adaptive system. For validation, we apply the adaptive technique on monostatic PolSAR imagery.

Because the decomposition essentially is a fitting to the PolSAR data, we compare the inner product between data and the individual polarimetric scattering models [47], leading to the following binary decision on the covariance data:

$$\frac{T_{11}}{T_{22}+T_{33}} \underset{needles}{\overset{disks}{\gtrless}} \frac{\sqrt{17}-\sqrt{2}}{7\sqrt{2}-2\sqrt{17}} \approx 1.64, \tag{74}$$

where T stands for the covariance matrix elements in the Pauli basis. This works very well when the random volume scattering is dominant.

We use an X-band PolSAR image acquired by DLR's F-SAR system [48] near Kaufbeuren, Germany, to demonstrate the different polarimetric features between coniferous forest and deciduous forest. The image has been multilooked for speckle suppression using an adaptive speckle filter [49]. One F-SAR scene is shown in Fig.15 as Pauli-basis pseudocolor composition along with the corresponding optical image (from Google Earth). The PolSAR image was collected in June 2010, whereas the optical image was collected in April 2018. By visual inspection, they match very well with each other on land cover. The deciduous stands are clearly visible from the optical image as the brownish-colored top portion of the forest

area where the deciduous trees had not fully leafed. Over the same stands, the F-SAR image appears blueish associated with high |HH+VV| levels, which would suggest a strong odd-bounce scattering. At X-band, we expect the primary scattering is due to random vegetation scatterers. The standard needle model cannot explain this observation, whereas the random disk model clearly predicts a significantly higher |HH+VV| level.

Figure 15(c) shows the copolar correlation coefficient on this F-SAR image and Fig. 15(d) shows the decision map based on Eq. (74). The deciduous stands have much higher correlation than the coniferous stands. The random disk model correctly predicts the observed correlation coefficient at 0.75 as compared to 0.33 by the random needle model. The city blocks on the top right part of the image also show higher copolar correlations; these arise from the rank-1 ground scattering mechanisms, either double-bounce scattering at building edges or rough surface scattering. In the forest area, the decision map maintains a good agreement with the deciduous stands.

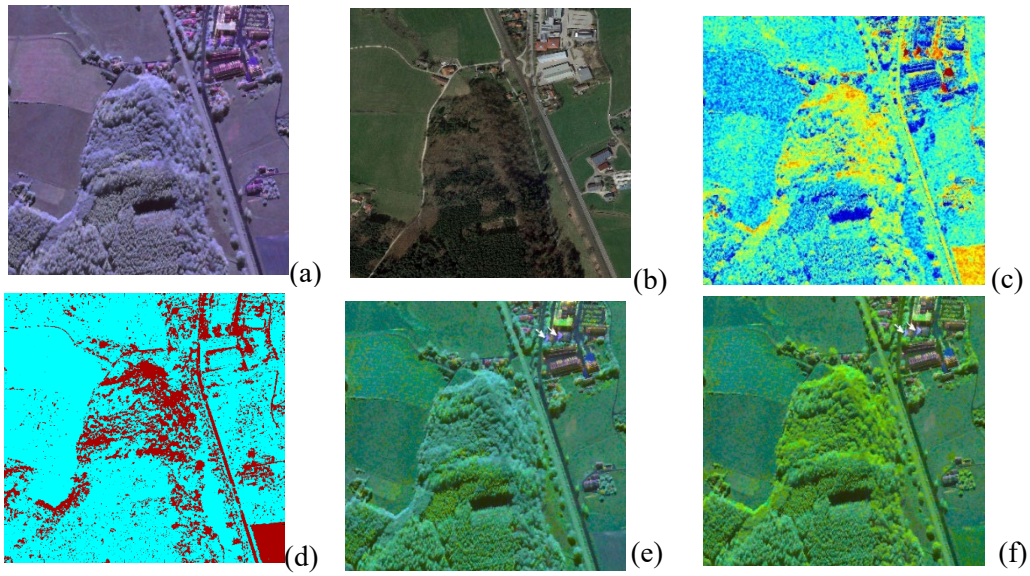

Fig 15—The radar beam is incident from the top of the image. Test site imagery: (a) F-SAR image in Pauli-basis pseudocolor composition, and (b) the collocated optical image.

The standard Freeman-Durden decomposition does not account for possible random disk scatterers. The decomposition results are shown in Fig.15(e) using the standard random needle model alone and in Fig.15(f) using the adaptive decision with the random disk model included. There is a big difference in the appearance of the deciduous stands. Using the standard model, they appear bluish in the classification map, similar to the Pauli basis decomposition. This is because scattering from the random disks has higher |HH+VV| levels such that the residual, after removal of the volume-scattering component, has a significant presence in the odd-bounce channel. Using the revised model, they appear much greener, revealing higher-volume scattering power, for which the observed |HH+VV| signal is accounted for by the random disks. Quantitatively, the power assigned to the random-volume component is much higher for those stands using the revised model. For the deciduous stands in the forest area, the estimated volume-scattering fraction increases by 27%, on average.

Other advanced decision criteria can be adopted for model selection between different vegetation scatter types, for example, using a recent approach based on an L_1 regularization term [41]. We use this simple binary decision to verify our random spheroid-based volume scattering model with data.

4.3 Rough Surface Scattering and Parameter Estimation

4.3.1 Extended-Bragg Scattering Model

Polarimetric radar return from rough terrain surface is dependent on multiple factors, such as the soil permittivity, the surface roughness, the terrain slope, the radar look angle, and in particular to bistatic SAR, the sensing geometry. Surface roughness is a critical factor, allowing the scattering response to be received in any direction, but also a nuisance to soil moisture retrieval. Especially as roughness increases, the SPM formulation described earlier for surface scattering becomes insufficient. It has been a long effort to develop advanced scattering models that are applicable to general rough surface conditions [21, 50–53]. Among them, the extended-Bragg (X-Bragg) model is appealing to polarimetric radar observations by explicitly expressing the roughness-induced random polarization orientation angle (POA) variation [50].

It is well known that the surface orientation affects the characteristic polarization angles in the scattered return, as exemplified in Eqs. (60)–(62). Roughness results in an incoherent sum of multiple scatter elements of distinct polarization angles. Also recall Eq. (59) and note that $\phi_s = 180^\circ$ in the monostatic case. Therefore, there exists an alignment of polarization states that makes the scattering matrix diagonal, which we call the principal plane. The POA angle is a function of radar incidence angle and the surface orientation angles and the X-Bragg model describes its variation.

In the bistatic case, ϕ_s takes arbitrary values and is coupled with both surface orientation angles and the beam geometry. The POA angles that can diagonalize the bistatic scattering matrices are then related to all the surface parameters, not just to the surface orientation. Therefore, we cannot separate out the surface orientation factors from the principal plane scattering. Instead, we need to revise the X-Bragg model to account for all the entangled dependence. We develop a bistatic X-Bragg model that is built on random surface orientation angles for a random sample of SPM facets.

To describe the surface orientation variation, we use von Mises_Fisher (vMF) distribution that is fit to describe a unimodal directional distribution with cyclic angular variables [54]. The random surface orientation angles θ_n and ϕ_n would follow

$$f(\theta_n, \phi_n; \kappa) = Ce^{\kappa \cos\theta_n},\ 0 \le \theta_n \le \pi/2, \tag{75}$$

where κ is a concentration parameter that controls the spread of the distribution, with a large value for a narrow distribution, and C is a normalization constant. It can be found that

$$C = \frac{\kappa \exp(-k/2)}{4\pi \sinh(\kappa/2)} \tag{76}$$

for the specified domain. The concentration parameter κ likely ranges from 15 to 100 through a simulation study, showing that the corresponding polarimetric entropy ranges from 0.1 (indicating a random scattering process) to 0.01 (indicating a coherent scattering process).

Next, we can evaluate the local beam angles using Eqs. (57)–(59), the POAs using Eqs. (60)–(61), and the scattering matrix using Eq. (56). The absolute scattering phase is also random due to the scatter position in a resolution cell. The covariance matrix elements can be derived from a sample of the random scattering matrices. If the speckle effect is not of concern, we can also directly evaluate their theoretical values using integration based on the vMF distribution according to

$$\langle s_{pq} s_{uv}^* \rangle = \iint s_{pq}(\theta_n, \phi_n; \varepsilon_r) s_{uv}^*(\theta_n, \phi_n; \varepsilon_r)\, f(\theta_n, \phi_n; \kappa) \sin\theta_n\, 1_n(\theta_n, \phi_n) d\theta_n d\phi_n, \tag{78}$$

where 1_n is an indicator function for beam blockage defined as

$$1_n(\theta,\phi) = \begin{cases} 1 & (\theta,\phi) \in \left\{\theta_n,\phi_n | 0 \le \theta_i < \frac{\pi}{2}, 0 \le \theta_s < \frac{\pi}{2}\right\} \\ 0 & \text{otherwise} \end{cases}. \tag{79}$$

The X-Bragg model is useful in the monostatic mode to analyze the orientation factor incurred by surface slopes. In monostatic geometry, the surface orientation contributes to both the POA and the local incidence angle (LIA), but their variation can be treated as nearly separable. Figure 16 shows the marginal distribution of POA and LIA derived from vMF-distributed surface orientation angles. Within the common range of radar look angles (e.g., other than the steep incidence), both the POA variation and the LIA variation are Gaussian-shaped; the LIA variation is nearly constant and independent of the POA variation. The POA variation can be evaluated from monostatic PolSAR observation. If the mean surface slope is known, it can further lead to the randomness measure on the surface orientation.

The LIA variation along with the soil permittivity and the roughness spectrum give rise to the variation of the principal scattering features. The original X-Bragg model only accounts for the soil permittivity in its principal-plane-scattering evaluation. Using simulated datasets based on the revised X-Bragg model, we find that overlooking the LIA variation effect leads to a significant overestimation on the permittivity, with larger biases for the case of smaller κ. The bias can reach up to 100% when $\kappa < 40$ at moderate radar look angles.

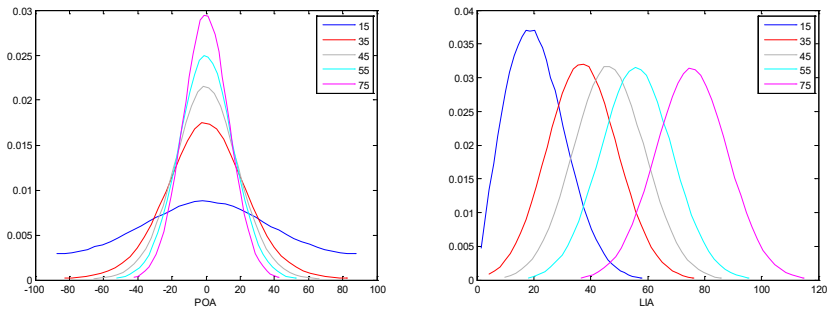

Fig. 16—The marginal distribution of POA (left) and LIA (right) incurred by random surface orientation. The orientation distribution follows a vMF distribution with $\kappa = 20$. The line colors mark for different radar look angles.

4.3.2 Two-Scale Rough Surface Scattering Model

The revised X-Bragg model improves the orientation related modulation in the bistatic scattering response. However, the scattering amplitude also varies with the LIA as well as the surface roughness spectrum. The full SPM scattering formation can be expressed in [55]

$$s_{pq}(\varepsilon_r;\theta_i,\theta_s,\phi_s) = k_0^2 \cos\theta_i \cos\theta_s \, W^{\frac{1}{2}}\left(\bar{k}_{\rho s} - \bar{k}_{\rho i}\right)(1-\varepsilon_r)\, g_{pq}(\varepsilon_r;\theta_i,\theta_s,\phi_s)\,, \tag{80}$$

where subscripts p and q respectively denote the receiving polarization and the illuminating polarization, k_0 is the wavenumber, W is the surface roughness spectrum, $\bar{k}_\rho$ is the horizontal component of the wavevectors, and g stands for the SPM scattering kernels. For Gaussian roughness spectrum, W can be written as

$$W(k) = \frac{1}{2}L^2 \exp\left(-\frac{L^2k^2}{4}\right), \tag{81}$$

where L is the correlation length and k is modified by the scattering geometry as

$$\bar{k}_{\rho s} - \bar{k}_{\rho i} = k_0 \cdot \left[\hat{k}_s - \hat{k}_i - (\cos\theta_{\mathrm{i}} + \cos\theta_s)\hat{n}\right]. \tag{82}$$

The two-scale rough surface scattering model (TSM) treats the surface roughness in two separable scales [56]. At the small scale, the surface condition in an elementary facet satisfies the SPM assumption, with variation horizontally on the order of wavelength and vertically much smaller than wavelength; its scattering amplitude depends on the roughness spectrum and the local beam angles. At the large scale, the facets have random orientation, with variation vertically on the order of wavelength or higher; its polarimetric feature significantly changes.

The TSM highlights an additional challenge for physical rough surface retrievals using PolSAR observations. It introduces extra roughness parameters to account, with the small-scale roughness characterized by the roughness spectrum and the correlation length. Provided that we know the true roughness spectrum function, we can build an optimization-driven parameter-estimation process based on the TSM formulation. However, in theory, it will be a major hurdle if the natural terrain features various types of roughness spectrum.

To verify the spectrum role, we evaluated the variability on the solution space due to potential spectrum uncertainty in the monostatic mode. We simulate a horizontal, rough-surface case under an incidence angle of 55°. The relative permittivity of soil varies in a range from 2 to 22 and the orientation concentration parameter κ varies in a range from 15 to 500. Let the POA be τ and the ellipticity angle be ϵ. In the Pauli basis, if the principal plane scattering features s_t and s_d, the scattering vector can be written as

$$\mathbf{v}_p = \begin{bmatrix} 1 & 0 & 0 \\ 0 & \cos 2\tau & -\sin 2\tau \\ 0 & \sin 2\tau & \cos 2\tau \end{bmatrix} \begin{bmatrix} \cos 2\epsilon & 0 & j\sin 2\epsilon \\ 0 & 1 & 0 \\ j\sin 2\epsilon & 0 & \cos 2\epsilon \end{bmatrix} \begin{bmatrix} s_t \\ s_d \\ 0 \end{bmatrix}, \tag{83}$$

and its covariance matrix follows $\mathbf{T} = \langle \mathbf{v}_p \mathbf{v}_p^H \rangle$. In general, ϵ is close to zero. Then, we have the following roll-invariant term

$$ALF = \tan^{-1}\sqrt{(T_{22} + T_{33})/T_{11}} \tag{84}$$

that is independent of the POA variation. The POA variation can be evaluated from

$$\rho_4 = \langle \cos 4\tau \rangle = (T_{22} - T_{33})/(T_{22} + T_{33}). \tag{85}$$

The pair of ρ_4 and ALF act on different variation dimensions, and together, they construct the solution space (through a look-up table) for the original X-Bragg model, as demonstrated in Fig. 17(a). However, due to LIA-induced modulation on the principal scattering features, the small-scale roughness makes a big difference, as shown in Fig. 17(b,c), under different roughness characteristics. Combinations of other principal scattering variables also show solution space shifts. Resolving this uncertainty requires additional constraints, which bistatic or multistatic observations may provide. However, currently we lack field data to further such development.

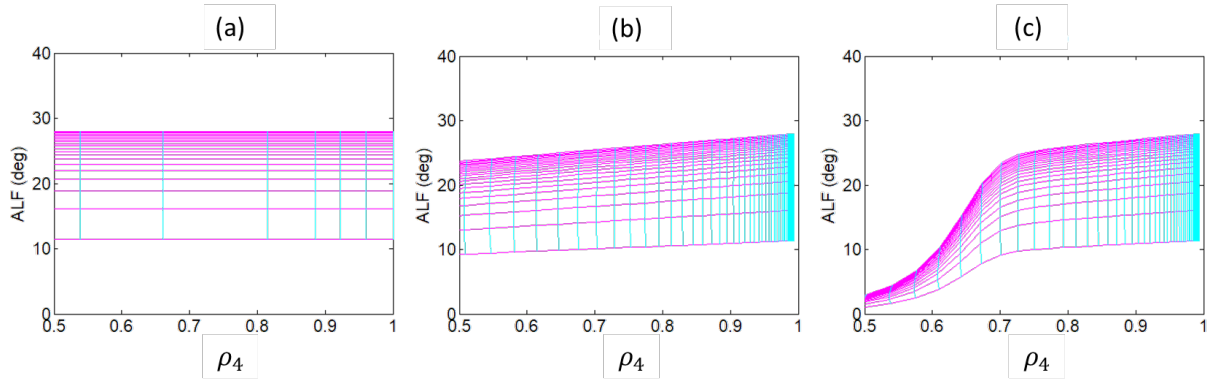

Fig. 17—The ρ_4- *ALF* space of varying orientation randomness and varying relative permittivity, when (a) the LIA variation is not accounted for, (b) the LIA variation is accounted for Guassian roughness spectrum ($L = 0.1\lambda$), and (c) the LIA variation is accounted for fractal roughness spectrum (Hurst exponent = 0.8).

4.3.3 Rough Surface Parameter Estimation

Modeling the bistatic rough surface scattering is highlighted by the deep coupling across the geometry factors and the roughness characteristics. Following on this, we revisited the monostatic case and tested the key aspects of the new development on legacy monostatic PolSAR imagery. We selected a case of mountainous terrain observation collected by NASA/JPL's L-band UAVSAR system near Camp Roberts, California, which features rolling hills with light vegetation. The PolSAR product was multilooked using 3 pixels in azimuth and 12 pixels in range, delivering a resolution of 7 m in azimuth and 5 m in range, approximately. We suppress SAR speckle further using a nonlocal speckle filter [57] with a 3×3 patch-based test. The final resolution is comparable to that of the DEM product we used.

First, we reinvestigated POA estimation to retain the ellipticity angles. Fig. 18(a) shows a Pauli-basis composite image of the selected scene. The radar beam steers from top to bottom of the image while the UAVSAR platform moves from left to right. The aircraft headed northeast at 50.3° azimuth angle. Fig. 18(b) presents the co-registered DEM map using NASA's 1-arc-second SRTM product where the mountainous terrain is clearly appreciable. In the valleys and some hillsides, the Pauli-basis composition indicates the dominant presence of forest cover, where POA will be noisy and even possibly not reflective of the terrain slopes. In [58] was given a detailed evaluation on the effect of volume scattering on POA estimation. To limit our comparison to the regions of dominant surface scattering, we use the radar vegetation index (RVI) [59],

$$RVI = \frac{4\lambda_3}{\lambda_1+\lambda_2+\lambda_3}, \tag{86}$$

where λ stands for the eigenvalues and the subscript number marks for the descending order by imposing the restriction of RVI<0.5.

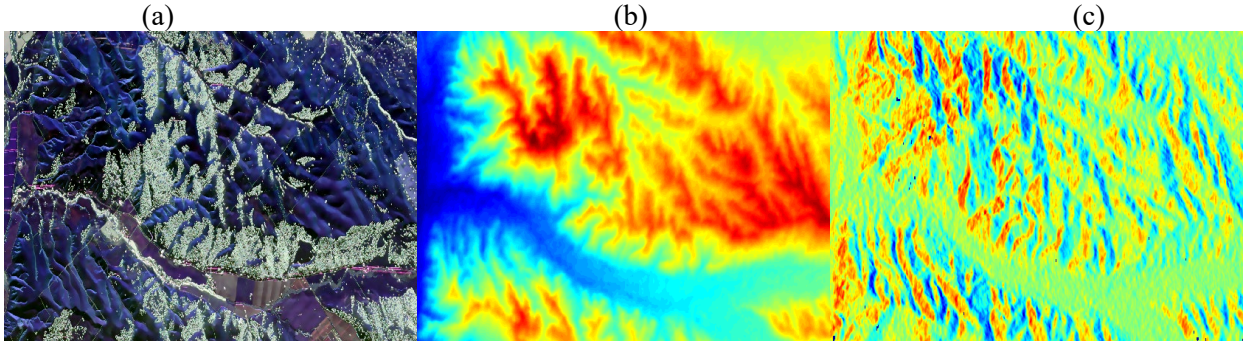

Fig. 18—(a) L-band UAVSAR image near Camp Roberts, California, color-coded in the Pauli basis, (b) the co-registered SRTM DEM map, (c) the derived polarization orientation angles. From top to bottom is the slant range direction.

From the DEM map, we evaluated the terrain slopes in terms of the local altitude gradients in the longitude direction, z_x, and in the latitude direction, z_y. The look angle η was derived from the co-registered altitude and the radar position. For this left-looking SAR moving toward azimuth angle ψ, the slope-induced POA follows

$$\tan\theta = \frac{z_x \sin\psi + z_y \cos\psi}{\sin\eta + z_x \cos\psi \cos\eta - z_y \sin\psi \cos\eta}. \tag{87}$$

Figure 18(c) presents the derived POA image that serves as the ground truth.

We take the general scattering vector Eq. (83) to expand the covariance elements as follows:

$$T_{11} = \cos^2 2\epsilon \langle |s_t^2| \rangle; \tag{88}$$

$$T_{22} = \langle \sin^2 2\tau \rangle \sin^2 2\epsilon \langle |s_t^2| \rangle + \langle \cos^2 2\tau \rangle \langle |s_d^2| \rangle + \langle \sin 4\tau \rangle \sin 2\epsilon \, \Im\langle s_t s_d^* \rangle; \tag{89}$$

$$T_{33} = \langle \cos^2 2\tau \rangle \sin^2 2\epsilon \langle |s_t^2| \rangle + \langle \sin^2 2\tau \rangle \langle |s_d^2| \rangle - \langle \sin 4\tau \rangle \sin 2\epsilon \, \Im\langle s_t s_d^* \rangle; \tag{90}$$

$$T_{12} = \langle \cos 2\tau \rangle \cos 2\epsilon \langle s_t s_d^* \rangle + j \langle \sin 2\tau \rangle \sin 4\epsilon \langle |s_t^2| \rangle / 2; \tag{91}$$

$$T_{13} = \langle \sin 2\tau \rangle \cos 2\epsilon \langle s_t s_d^* \rangle - j \langle \cos 2\tau \rangle \sin 4\epsilon \langle |s_t^2| \rangle / 2; \tag{92}$$

$$T_{23} = \langle \sin 4\tau \rangle \langle |s_d^2| \rangle / 2 - \langle \sin 4\tau \rangle \sin^2 2\epsilon \langle |s_t^2| \rangle / 2 - \langle \cos 4\tau \rangle \sin 2\epsilon \, \Im\langle s_t s_d^* \rangle - j \sin 2\epsilon \, \Re\langle s_t s_d^* \rangle. \tag{93}$$

The orientation angle τ is randomly distributed for distributive surface facets, whereas the ellipticity angle is set as a deterministic variable since its presence mainly indicates the deviation from symmetric backscatter. By setting $\epsilon = 0$, the mean POA can be derived from Eqs. (89), (90), and (93), reaching the widely used solution

$$\bar{\tau} = 0.25 \arg\{(T_{22} - T_{33}) + j2\Re(T_{23})\}. \tag{94}$$

For nonzero τ, we attain a new solution from Eqs. (91) and (92) as

$$\bar{\tau} = 0.5 \tan^{-1}\{\Re(T_{13})/\Re(T_{12})\}. \tag{95}$$

For convenience, we refer to Eq. (94) as T_{23}-POA and to Eq. (95) as T_{13}-POA. The latter one does not work at the extreme ellipticity values of $\pm 45°$, but it corresponds to helix scattering with undefined orientation angle.

Figure 19(a) and Fig. 19(b) show the estimated T_{23}-POAs and T_{13}-POAs, respectively, for this case. The noisy results associated with vegetation (RVI>0.5) have been masked out. Both PolSAR estimations clearly reveal the mountainous terrain, but the latter shows a better correlation with the DEM-derived POA. Particularly, the former apparently suffers from a significant underestimation. In order to gain a quantitative measure on the different estimates, we draw their scatter plots against the DEM-derived POA, visualized in Fig.19(c, d) as two-dimensional distribution density. The linear fitting over the T_{23}-POAs shows a much larger deviation from the ideal line than the one over the T_{13}-POAs.

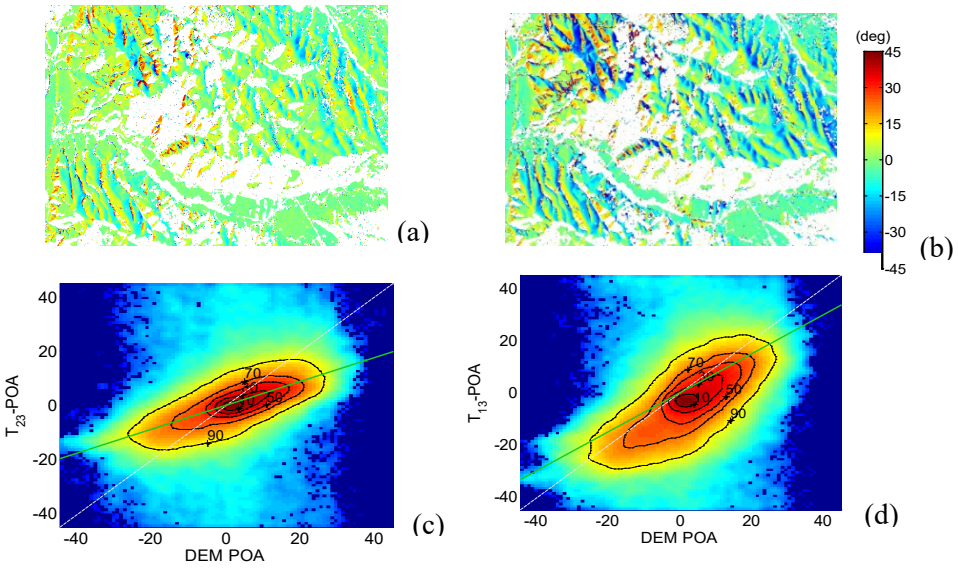

Fig. 19—The mean POA maps estimated from T_{23}-POA (a) and T_{13}-POA (b); and the density distribution between the DEM-derived POA (x-axis) and the estimated POA (y-axis) using T_{23}-POA (c) and T_{13}-POA (d)

Using the estimated $\bar{\tau}$, we can remove the mean POA from the polarimetric data and acquire "deoriented" covariance matrix $\mathbf{T}'$. Then, the ellipticity angle and the POA variation can be assessed with

$$\tan^2(2\epsilon) = \frac{\Im(T'_{13})\Im(T'_{23})}{T_{11}\Re(T'_{12})}, \tag{96}$$

$$\rho_4 = \frac{T'_{22}-T'_{33}}{-2\tan^2(2\tau)T_{11}+T'_{22}+T'_{33}}. \tag{97}$$

The majority of the estimated ellipticity angles fall below 3.4°, indicating negligible helicity in the scattering response. It is surprising to observe the big difference between the POA estimates in Fig.19. We determine that as the main reason the T_{23}-POA estimation essentially acts on the terms of $\langle|s_d^2|\rangle$, which can be negatively biased due to the presence of a double-bounce component. The estimated ρ_4 can serve as a quality indicator on the estimated POA. If the orientation distribution has wide spread, the mean POA estimate is subject to greater uncertainty. In this scene, the estimated ρ_4 is primarily positive, with a small amount of negative values interspersing in the forested areas and their edges. Those with negative ρ_4 estimates are discarded as non-surface-scattering pixels.

We can proceed to estimate the principal-plane polarimetric variables, including $\langle|s_t^2|\rangle$, $\langle|s_d^2|\rangle$, and $\langle s_t s_d^*\rangle$. Following the lead in [50], the relative permittivity can be retrieved using a precomputed lookup table. The estimated ε_r is presented in Fig. 20. Using the original X-Bragg model in which the LIA variation

is ignored, the estimation results in many large values that are apparently high for this arid landscape. If we apply the LIA variation to the model, assuming a Gaussian roughness spectrum with short correlation length, the estimation returns generally reasonable values. According to our finding, the estimation is sensitive to the small-scale roughness characteristics and the monostatic data lack additional constraints. Thus, this experiment mainly serves as a demonstration of the impact of LIA variation in the rough surface scattering.

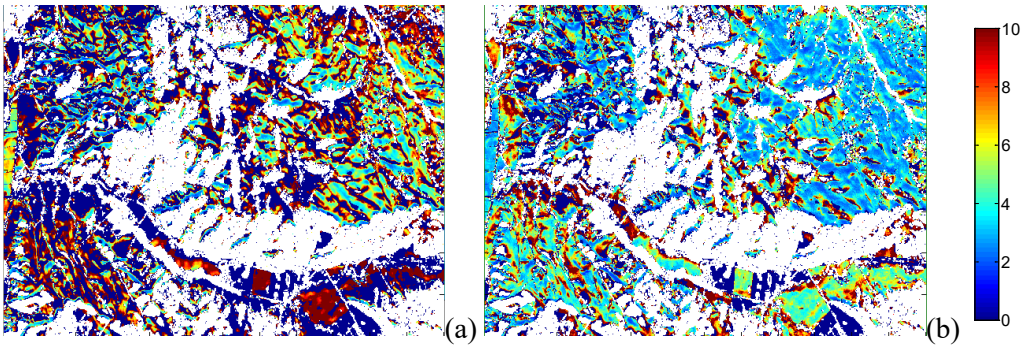

Fig. 20—The magnitude of estimated ε_r based on the X-Bragg model with the LIA variation ignored (a) and with the LIA variation incorprated (b). The dark-blue color indicates invalid solution to the scattering models.

5 SENSITIVITY AND IMAGING GEOMETRY

BiSAR operation introduces an extra, important design parameter to mission planning. Amid unrestrictive bistatic geometries, we desire to adopt a bistatic configuration that can improve the data utility to the utmost extent. This obviously depends on the specific sensing objective or the specific type of in-scene targets. For example, to simplify the forest scattering model in decomposition, we may set the bistatic angle to 90°, as implicated in Eqs. (67)–(69). In this section, we focus on rough surface sensing with a goal to get better measurement of the soil moisture contents (SMC). A favorable configuration arises when the sensitivity to soil moisture increases while the impact from roughness is relatively small.

According to earlier sensitivity studies, SAR intensities acquired near the forward specular direction are better suited than the backscatter observations to soil moisture estimation by virtue of a reduced dependence on surface roughness [60–62]. GPS reflectance data showed strong correlation between specular radar returns and field soil-moisture measurements [63]. However, the resolution becomes much poorer in the specular geometry. We want to extend the sensitivity evaluation to polarimetric variables. It is evident from 3.4 that for a slightly rough surface, the SPM formulation applies and the roughness factor can be removed by using polarimetric observations. As a polarimetric system collects rich scattering information using multiple polarization channels, we desire to explore whether some polarimetric variables are potentially advantageous to mitigate the roughness factor in soil moisture retrieval.

We note that with a fully polarimetric SAR, many combinations of the polarization channels are available. The choice of polarimetric combinations should also be physically meaningful and we use the observations represented in the standard reference system that allows evaluation of the cross-polarization scatter signatures. A list of ratios and correlation terms are defined straightforwardly over those polarization channels, as shown in Table 2. Additionally, we list in Table 3 a set of characteristic polarimetric variables that are independent of the polarization bases.

Table 2—The List of Direct Polarimetric Variables

$\langle\|HH\|^2\rangle$	$\langle\|VH\|^2\rangle/\langle\|HH\|^2\rangle$ ρ_{VHHH}	$\langle\|HV\|^2\rangle/\langle\|HH\|^2\rangle$ ρ_{HVHH}	$\langle\|VV\|^2\rangle/\langle\|HH\|^2\rangle$ ρ_{VVHH}
-	$\langle\|VH\|^2\rangle$	$\langle\|VH\|^2\rangle/\langle\|HV\|^2\rangle$ ρ_{VHHV}	$\langle\|VH\|^2\rangle/\langle\|VV\|^2\rangle$ ρ_{VHVV}
-	-	$\langle\|HV\|^2\rangle$	$\langle\|HV\|^2\rangle/\langle\|VV\|^2\rangle$ ρ_{HVVV}
-	-	-	$\langle\|VV\|^2\rangle$

Table 3—The List of Characteristic Polarimetric Variables

p_1 $\tau_{1i,s}, \epsilon_{1i,s}, \Gamma_1, \psi_1$	p_2/p_1	p_3/p_1	p_4/p_1
-	p_2 $\tau_{2i,s}, \epsilon_{2i,s}, \Gamma_2, \psi_2$	p_3/p_2	p_4/p_2
-	-	p_3 $\tau_{3i,s}, \epsilon_{3i,s}, \Gamma_3, \psi_3$	p_4/p_3
-	-	-	p_4 $\tau_{4i,s}, \epsilon_{4i,s}, \Gamma_4, \psi_4$

The scattering response is highly nonlinear. A complete characterization would need to evaluate its slope at various combinations of those surface moisture and roughness parameters. To make the evaluation tractable, we may use averages or approximations at some selected baseline settings. In [61], a quality factor was adopted to measure the balance between the moisture effect and the roughness effect on the bistatic observations. For a variable x, the quality factor is defined as

$$I(x) = \frac{\Delta x/\Delta sm}{\Delta x/\Delta sm + \Delta x/\Delta rough}, \tag{98}$$

where $\Delta x/\Delta sm$ stands for the change rate on x as incurred by the difference in soil moisture and $\Delta x/\Delta rough$ for that as incurred by the difference in surface roughness. However, they have different units and their values would vary with the type of the used parameters.

Instead, we set a set of baseline parameters as listed in Table 4 between the low end, for which the moisture and the roughness are low, and the high end, for which the moisture and the roughness are high. Then, we evaluate the contribution factors by comparing the incurred changes between a pair of observations made among those baseline parameters. For SMC vs. small-scale roughness, we assess the change responding to SMC as

$$\Delta sm = \left|x_{SM2,L1} - x_{SM1,L1}\right| + \left|x_{SM2,L2} - x_{SM1,L2}\right| \tag{99}$$

and the change responding to the correlation length as

$$\Delta roug = \left|x_{SM1,L2} - v_{SM1,L1}\right| + \left|x_{SM2,L2} - v_{SM2,L1}\right|. \tag{100}$$

Then, we get a unitless quality factor from

$$I_{SM-L}(x) = \frac{\Delta sm}{\Delta sm + \Delta roug}. \tag{101}$$

Table 4—The Comparison Baseline Setting of Rough Surface Parameters

	SMC	L	κ
Baseline Low	15%	0.5λ	50
Baseline High	25%	0.1λ	30

Similarly, we can evaluate a quality factor for SMC vs the large-scale roughness, $I_{SM-\kappa}$, using the low-end and high-end parameters of SMC and κ.

For the evaluation, we run TSM-based simulation at different soil-moisture and surface-roughness levels. In the simulation, we assume an incidence angle of 30°, which corresponds to a typical illumination geometry from a spaceborne SAR, and we assume the scattered return from a horizontal, rough surface is received at various beam directions of θ_s and ϕ_s. The high baseline listed in Table 4 is adopted as the control parameter in the comparison study. To evaluate the moisture-induced changes, we compute the model predicts at SMC values of 15% ($\varepsilon_r = 9.2 - j0.5$) and 25% ($\varepsilon_r = 14.6 - j0.9$), whereas the roughness settings are fixed. The radar frequency is set at L-band. For the small-scale roughness, a Gaussian spectrum is assumed with the correlation length L varying between 0.5λ and 0.1λ. For the large-scale roughness, a vMF distribution is assumed on the surface orientation with the concentration parameter κ varying between 50 and 30.

Figure 21(a) depicts the changes in the normalized intensities as the soil moisture increases from 15% to 25%. We see only a small change in HH and VV for the majority of bistatic geometries. At the forward grazing directions, however, HH is diminished while VV is enhanced, both moderately but perceivably. Consistent increases are present on HV and VH in response to the higher SMC, indicating enhanced cross-polarization response to moist, rough surfaces.

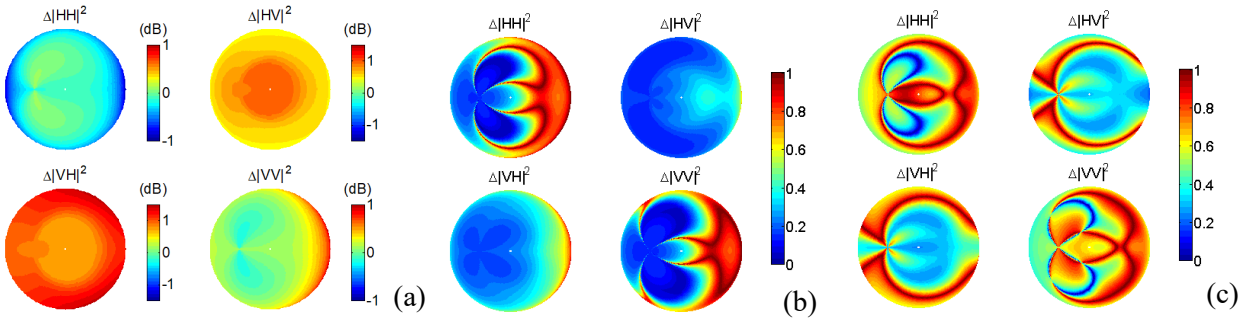

Fig. 21—Sensitivity evaluation on the normalized scattering intensities: (a) the changes due to SMC increases; (b) the quality factor I_{SM-L}; (c) the quality factor $I_{SM-\kappa}$.

As the small-scale roughness increases by reducing L from 0.5λ to 0.1λ, higher variations prevail in all polarimetric channels. Even though at the core, the SPM scattering from each individual facet is

independent of the small-scale roughness, collectively, due to the orientation effect from the large-scale roughness, the small-scale roughness will be reflected in the scattering responses. Especially, both HV and VH experience much higher enhancement as the surface becomes rougher in the small-scale term; accordingly, in them we do not expect to get favorable sensitivity to SMC. Figure 21(b) presents the derived quality factor I_{SM-L} that compares the SMC-induced change against the L-induced change. The four polarization channels respond in different manners, but overall, the forward directions would be favorable.

As randomness increases in the surface orientation distribution by reducing κ from 50 to 30, the intensities in HH and VV largely remain at the same level except at the low grazing directions, whereas the intensities in HV and VH manifest a clear pattern of increasing at the geometries where the SPM predicts null returns. This testifies that the large-scale roughness is primarily responsible for distributing the scattered power to the cross-polarization channels. Figure 21(c) presents the derived quality factor $I_{SM-\kappa}$ that compares the SMC-induced change against the κ-induced change. Similarly, the forward scattering directions give better sensitivity in HH and VV to SMC, but not at very low grazing angles. The bistatic geometry with good sensitivity can also be extended to other nonspecular scattering directions using HV and VH, provided that their signals are strong enough.

By taking intensity ratios, we hope to get part of the roughness effect canceled. Figure 22(a) shows that the various ratios generally increase with SMC. In VV/HH, we can expect substantial increases in the grazing directions, especially in the forward geometry. In VH/HV, a moderate increase occurs only in the grazing directions other than the backward geometry. The biggest change occurs in VH/HH at nearly all scattering geometries.

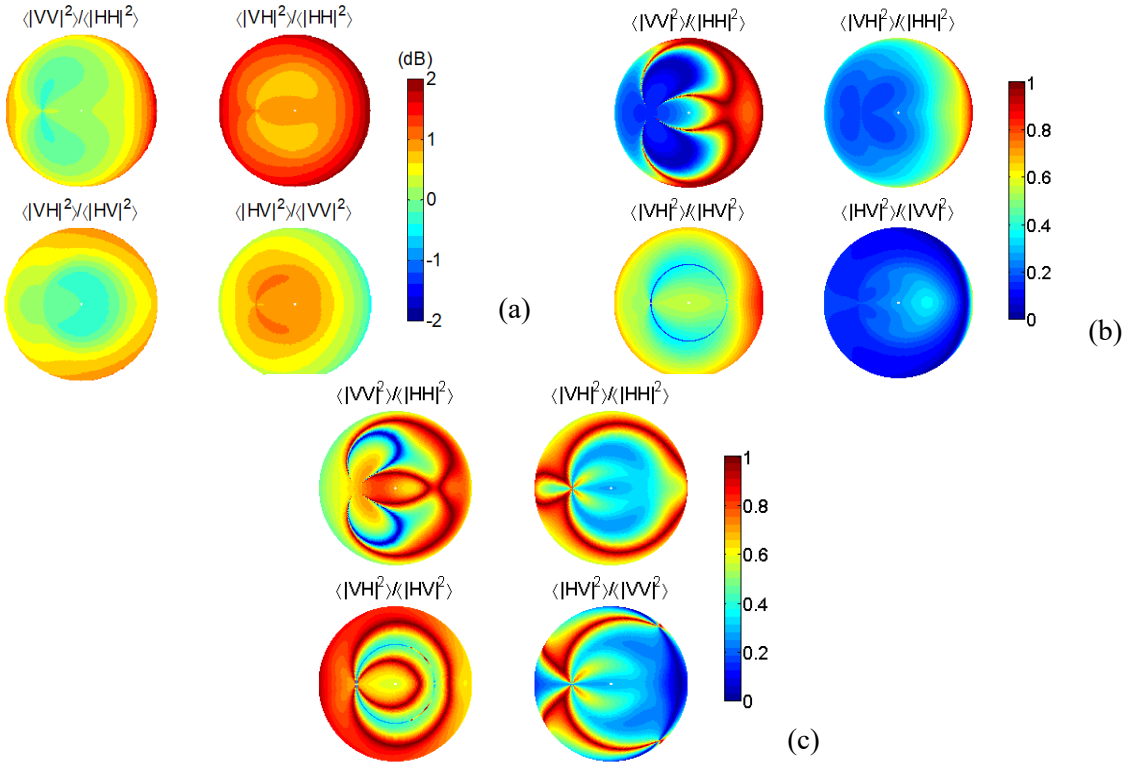

Fig. 22—Sensitivity evaluation on the scattering intensity ratios: (a) the changes due to SMC increases; (b) the quality factor I_{SM-L}; (c) the quality factor $I_{SM-\kappa}$.

In response to higher small-scale roughness, the VV/HH change is very small in the forward scattering directions. In VH/HV, there is barely any change, seemingly favorable, but meanwhile, the change due to higher SMC is also small. In the other ratios involving VH or HV, the changes generally are very large, apparently implying poor sensitivity to SMC. The quality factors shown in Fig. 22(b) clearly summarize that only the geometry in the forward grazing directions can ensure good quality and sensitivity to SMC.

Those intensity ratios are relatively immune to the change of the large-scale roughness. Accordingly, as indicated in Fig. 22(c), they fare very well to the SMC variation in the presence of surface orientation variation. This agrees with the polarimetric advantages presented in the X-Bragg model [50].

We speculate that the major surface scattering information is contained in the dominant characteristic component, $\underline{\boldsymbol{S}}_1$. It features the polarization state in terms of the polarization orientation angles $\tau_{i,s}$ and the ellipticity angles $\epsilon_{i,s}$ as well as the scattering parameters in terms of the scattering ratio Γ and the skip angle ν. The ellipticity angles provide a primary indicator of asymmetrical scattering from the targets and the skip angles provide a primary indicator of the number of bounces. They do not have any desired sensitivity to either the moisture variation or the roughness variation.

The characteristic POAs are intriguing to use. On the one hand, they vary with the orientation factors of the system polarizations and of the scattering targets. On the other hand, they are also coupled with the scattering process itself, reflecting a strong dependence on SMC. Figure 23 illustrates this coupling clearly as the demonstrated changes arise solely from the SMC variation (panels a and b). They are fairly large near the forward grazing directions. When comparing against the changes due to higher small-scale roughness, we do see higher quality factors in the forward region (panels' c and d). When comparing against the changes due to higher orientation randomness, we actually get better quality factors in much wider sensing geometries other than the specular direction (panels e and f). A particular difficulty in using the orientation angles is we cannot ascertain that the mean surface slope is always horizontal.

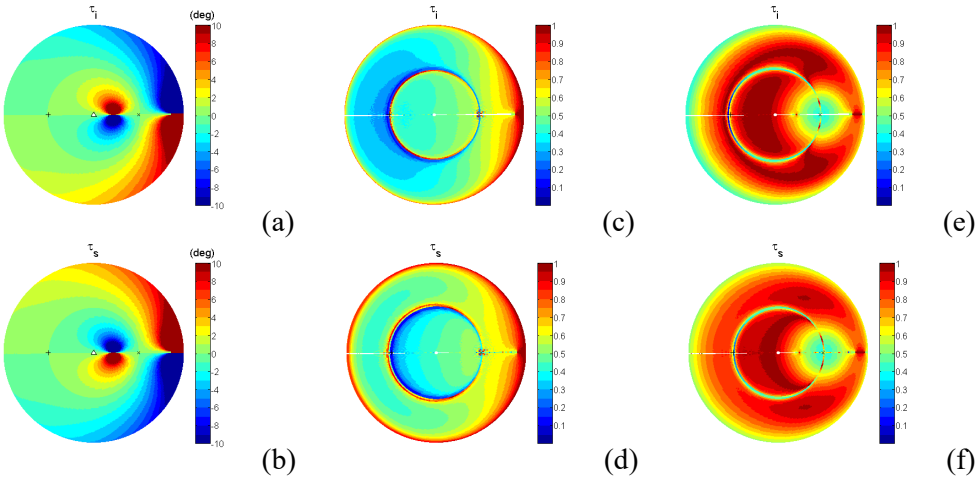

Fig. 23—Sensitivity evaluation on the characteristic polarization angles: (a,b) the changes due to SMC increases; (c,d) the quality factor I_{SM-L}; (e,f) the quality factor $I_{SM-\kappa}$.

The characteristic scattering ratio shown in Fig. 24(a) resembles the general trend of HH and VV intensities and their ratio VV/HH, implicating that it is capable of carrying the essential scattering information. However, the corresponding changes due to the surface roughness parameters are quite different. With the small-scale variation in terms of L, a large change exists in the backward directions,

whereas a small change exists in the forward directions. Accordingly, we see in Fig. 24(b) good sensitivity to SMC in a well-organized forward scattering region. With the large-scale variation in terms of κ, in the backward directions the associated change is also small, where Fig. 24(c) indicates good sensitivity to SMC. Altogether, they highlight a large sector of forward scatter geometries that is suitable for SMC measurement.

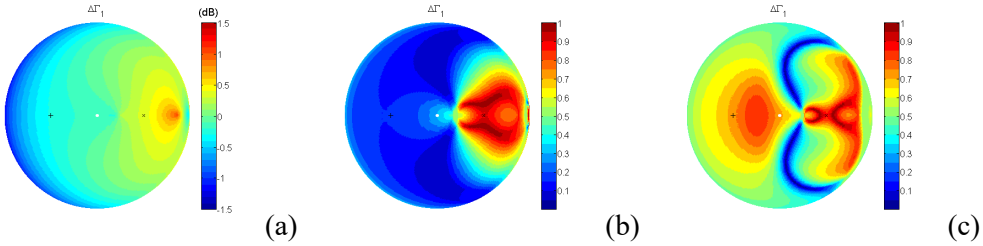

Fig. 24—Sensitivity evaluation on the characteristic scattering ratio: (a) the changes due to SMC increases; (b) the quality factor I_{SM-L}; (c) the quality factor $I_{SM-\kappa}$.

Overall, the optimal bistatic geometry is located near the specular direction and the forward grazing directions, especially for scattering intensities or their ratios. This agrees with the previous research findings. The agreement regardless of being based on different polarization reference systems is reasonable because they converge in the bistatic plane, which contains both the forward and the specular directions. However, we may venture to other nonspecular geometries using cross-polarization variables or characteristic polarization angles. The small-scale variation in terms of the correlation length is found more problematic for soil moisture retrieval unless the surface orientation variation is very small.

6 CONCLUSIONS

With this program, we investigated the polarimetric capability for bistatic SAR operation. Despite being entangled with the sensing geometry, bistatic polarimetric observations show promising advantages to improve the full determination of the target parameters. Built on the basic bistatic scattering models, we developed the fundamental polarimetric analysis approaches, the physical based target decomposition process, and the rough terrain parameter estimation algorithms. The development in this work will enable us to connect future bistatic polarimetric imagery with physical target features. We performed a sensitivity study for soil moisture retrieval, along the course demonstrating a geometry selection process for mission planning. It affirms the favorable geometry in the specular direction but also shows good sensitivity in other directions using cross-polarization channels and characteristic scattering parameters, demonstrating the value of using polarimetric variables to improve bistatic sensing. We also demonstrated the added value of fusing simultaneous monostatic polarimetric observations to estimate target parameters. We expect to collect full polarimetric datasets of simultaneous bistatic and monostatic operation in future field campaigns and apply the developed techniques in this program to real imagery.

REFERENCES

1. A. S. Goh, M. Preiss, and N. J. S. Stacy, “Initial polarimetric results from the Ingara bistatic SAR experiment,” 2013 International Conference on Radar, Adelaide, SA, Australia, 2013, pp.27-32.

2. A. Meta, C. Trampuz, A. Coccia, M. Ortolani, and R. Turtolo, "First results of the BelSAR L band airborne bistatic fully polarimetric Synthetic aperture radar campaign," 2014 IEEE Geosci. Remote Sens. Symp., Fort Worth, 2017, pp.1040-1042.
3. N. J. Willis, Bistatic Radar, 2nd ed. (SciTech Publishing, Inc., Raleigh, NC, 2005).

4. M. Cherniakov, Bistatic Radars: Emerging Technology (Wiley, New York, 2008).

5. J. S. Lee and E. Pottier, Polarimetric Radar Imaging from Basics to Applications (Boca Raton, FL, USA: CRC Press, 2009).

6. J. J. van Zyl and Y. Kim, Synthetic Aperture Radar Polarimetry (Wiley & Sons, Inc. Hoboken, New Jersey, 2011).

7. D. J. McLaughlin, Yuliang Wu, W. G. Stevens, Xuehu Zhang, M. J. Sowa, and B. Weijers, "Fully polarimetric bistatic radar scattering behavior of forested hills," IEEE Trans. Antennas Propagat., 50(2), 101-110 (2002).

8. J. R. Huynen, "Measurement of the target scattering matrix," Proc. IEEE, 53(8), 936–946 (1965).

9. H. Mott, Remote Sensing with Polarimetric Radar (Wiley & Sons, Inc. Hoboken, New Jersey, 2006).

10. E. Lüneburg and S. R. Cloude, "Bistatic scattering," Proc. SPIE, 3120, 56–68 (1997).

11. S. R. Cloude and E. Pottier, "A review of target decomposition theorems in radar polarimetry," IEEE Transaction on Geosci. Remote Sens., 34(2), 498-518 (1996).

12. A. L. Germond, E. Pottier, and J. Saillard, "Foundations of bistatic radar polarimetry theory," Radar 97, Edinburgh, UK, 1997, pp.833-837.

13. Z. H. Czyz, "On theoretical foundation of coherent bistatic radar polarimetry," Proc. SPIE, 3120, 69-105 (1997).

14. S. R. Cloude, "On the status of bistatic polarimetry theory," 2005 IEEE Geosci. Remote Sens. Symp., Seoul, 2005, pp.2003-2006.

15. I. Walterscheid, A. R. Brenner, and J. H. G. Ender, "Results on bistatic synthetic aperture radar," Electron. Lett., 40(19), 1224–1225 (2004).

16. J.J. van Zyl and F.T. Ulaby, Scattering matrix representation for simple targets. In Radar Polarimetry for Geoscience Applications, F.T. Ulaby and C. Elachi, Eds, p. 364. (Norwood, MA, Artech House, 1990).

17. V. N. Bringi and V. Chandrasekar, Polarimetric Doppler Weather Radar: Principles and Applications, (Cambridge, U.K.: Cambridge Univ. Press, 2001).

18. S. O. Rice, "Reflection of electromagnetic waves from slightly rough surfaces," Commun. Pure Appl. Math., 4(1-3), 361–378 (1951).

19. J. T. Johnson and J. Ouellette, "Polarization features in bistatic scattering from rough surfaces." IEEE Trans. Geosci. Remote Sens., 52, 1616-1626 (2014).

20. F. T. Ulaby, R. K. Moore and A. K. Fung, Microwave Remote Sensing: Active and Passive, from Theory to Applications (Artech House, Norwood, MA, 1986).
21. J. T. Johnson, "Third order small perturbation method for scattering from dielectric rough surfaces," J. Opt. Soc. Amer. A, 16(11), 2720–2726 (1999).

22. M. A. Karam, A. K. Fung, and Y. M. M. Antar, "Electromagnetic wave scattering from some vegetation samples," IEEE Trans. Geosci. Remote Sens., 26(6), 799-808 (1988).

23. M. Neumann, L. Ferro-Famil, and A. Reigber, "Estimation of forest structure, ground, and canopy layer characteristics from multi-baseline polarimetric interferometric SAR data," IEEE Trans. Geosci. Remote Sens., 48(3), 1086-1104 (2010).

24. M. Arii, J. J. van Zyl, and Y. Kim, "A general characterization for polarimetric scattering from vegetation canopies," IEEE Trans. Geosci. Remote Sens., 48(9), 3349-3357 (2010).

25. Y. Wang, T. L. Ainsworth, and J.-S. Lee, "Estimation of the orientation and shape parameters of canopy scatterers from POLSAR observations," IEEE J. Sel. Topics in App. Earth Obs. Remote Sens., 5(3), 835-847 (2012).

26. D. L. Schuler, J.-S. Lee, and G. De Grandi, "Measurement of topography using polarimetric SAR images," IEEE Trans. Geosci. Remote Sensing, 34(5), 1266-1277 (1996).

27. D. L. Schuler, J.-S. Lee, T. L. Ainsworth, and M. R. Grunes, "Terrain topography measurement using multipass polarimetric synthetic aperture radar data," Radio Science, 35(3), 813-832 (2000).

28. E. Pottier, D. L. Schuler, J.-S. Lee, and T. A. Ainsworth, "Estimation of the terrain surface azimuthal-range slopes using polarimetric decomposition of POLSAR data," 1999 IEEE Geosci. Remote Sens. Symp., Hamburg, Germany, 1999, 2212–2214.

29. J.-S. Lee, D. L. Schuler, and T. L. Ainsworth, "Polarimetric SAR data compensation for terrain azimuth slope variation," IEEE Trans. Geosci. Remote Sens., 38(5), 2153–2163 (2000).

30. J.-S. Lee, D. L. Schuler, T. L. Ainsworth, E. Krogager, D. Kasilingam, and W. M. Boerner, "On the estimation of radar polarization orientation shifts induced by terrain slopes," IEEE Trans. Geosci. Remote Sens., 40(1), 30–41 (2002).

31. J.-S. Lee and T. L. Ainsworth, "The effect of orientation angle compensation on coherency matrix and polarimetric target decompositions," IEEE Trans. Geosci. Remote Sens., 49(1), 53-64 (2011).

32. J. J. van Zyl, H. A. Zebker, and C. Elachi, "Imaging radar polarization signatures," Radio Science, 22, 529-543 (1987).

33. J. J. van Zyl, "Application of Cloude's target decomposition theorem to polarimetric imaging radar," SPIE, 127, 184-212 (1992).

34. S. R. Cloude and E. Pottier, "The concept of polarization entropy in optical scattering," Optical Engineering, 34(6), 1599-1610 (1995).

35. S. Allain, C. Lopez-Martinez, L. Ferro-Famil, and E. Pottier, "New eigenvalue-based parameters for natural media characterization," 2005 IEEE Geosci. Remote Sens. Symp., Seoul, Korea, 2005, pp.40-43.

36. R. Touzi, "Target scattering decomposition in terms of roll-invariant target parameters," IEEE Trans. Geosci. Remote Sensing, vol. 45, pp. 73-84, Jan 2007.

37. A. Freeman and S. L. Durden, "A three-component scattering model for polarimetric SAR data," IEEE Trans. Geosci. Remote Sens., 36(3), 963–973 (1998).

38. Y. Yamaguchi, T. Moriyama, M. Ishido, and H. Yamada, "Four component scattering model for polarimetric SAR image decomposition," IEEE Trans. Geosci. Remote Sens., 43(8), 1699-1706 (2005).

39. S.-W. Chen, X.-S. Wang, S.-P. Xiao, and M. Sato, "General polarimetric model-based decomposition for coherency matrix," IEEE Trans. Geosci. Remote Sens., 52(3), 1843-1855 (2014).

40. Y. Cui, Y. Yamaguchi, J. Yang, H. Kobayashi, S.-E. Park, and G. Singh, "On complete model-based decomposition of polarimetric SAR coherency matrix data," IEEE Trans. Geosci. Remote Sens., 52(4), 1991-2001 (2014).

41. T. L. Ainsworth, Y. Wang, and J. -S. Lee, "Model-based polarimetric SAR decomposition: an L1 regularization approach," IEEE Trans. Geosci. Remote Sens., 60, 1-13 (2022).

42. J.-S. Lee, T. L. Ainsworth, and Y. Wang, "Generalized polarimetric model-based decompositions using incoherent scattering models," IEEE Trans. Geosci. Remote Sens., 52(5), 2474-2491 (2014).

43. J. J. van Zyl, K. Yunjin, and M. Arii, "Requirements for model-based polarimetric decompositions," 2008 IEEE Geosci. Remote Sens. Symp., Boston, MA, Jul. 7-11, 2008, pp.V417-V420.

44. J. J. van Zyl, M. Arii, and Y. Kim, "Model-based decomposition of polarimetric SAR covariance matrices constrained for nonnegative eigenvalues," IEEE Trans. Geosci. Remote Sens., 49(9), 3452–3459 (2011).
45. D. M. Wiberg, State space and linear system, McGraw-Hill (1971).

46. J. E. Prussing, "The principal minor test for semidefinite matrices," AIAA J. Guidance Control Dynamics, 9(1), 121-122 (1986).

47. D. Ratha, A. Bhattacharya, and A. C. Frery, "Unsupervised classification of PolSAR data using a scattering similarity measure derived from a geodesic distance," IEEE Geosci. Remote Sens. Lett., 15(1), 151-155 (2018).

48. A. Reigber et al., "Current status of DLR's new F-SAR sensor," 8th European Conference on Synthetic Aperture Radar, Aachen, Germany, 2010, pp.1-4.

49. Y. Wang, T. L. Ainsworth, and J.-S. Lee, "Application of Mixture Regression for Improved Polarimetric SAR Speckle Filtering," IEEE Trans. Geosci. Remote Sens., 55(1), 453-467 (2017).

50. I. Hajnsek, E. Pottier, and S. R. Cloude, "Inversion of surface parameters from polarimetric SAR," IEEE Trans. Geosci. Remote Sens., 41(4), 727–744 (2003).

51. A. G. Voronovich, "Small-slope approximation for electromagnetic wave scattering at a rough surface interface of two dielectric half-spaces," Waves Random Media, 4, 337–367 (1994).

52. K. S. Chen, Tzong-Dar Wu, Leung Tsang, Qin Li, Jiancheng Shi, and A. K. Fung, "Emission of rough surfaces calculated by the integral equation method with comparison to three-dimensional moment method simulations," IEEE Trans. Geosci. Remote Sens., 41(1), 90-101 (2003).

53. K. S. Chen, L. Tsang, K. -L. Chen, T. H. Liao, and J. -S. Lee, "Polarimetric simulations of SAR at L-band over bare soil using scattering matrices of random rough surfaces from numerical three-dimensional solutions of maxwell equations," IEEE Trans. Geosci. Remote Sens., 52(11), 7048-7058 (2014).

54. K. V. Mardia, Statistics of directional data (New York, Academic Press, 1972).

55. G. R. Valenzuela, "Theories for the interaction of electromagnetic and oceanic waves—A review," Boundary-Layer Meteorology, 13, 61–85 (1978).

56. A. Iodice, A. Natale, and D. Riccio, "Retrieval of soil surface parameters via a polarimetric two-scale model," IEEE Trans. Geosci. Remote Sens., 49, 2531-2547 (2011).

57. Jiong Chen, Y. Chen, W. An, Y. Cui, and J. Yang, "Nonlocal filtering for polarimetric SAR data: a pretest approach." IEEE Trans. Geosci. Remote Sens., 49, 1744-1754 (2011).

58. J.-S. Lee, T. L. Ainsworth, and Y. Wang, "Polarization orientation angle and polarimetric SAR scattering characteristics of steep terrain," IEEE Trans. Geosci. Remote Sens., 56(12), 7272-7281 (2018).

59. Y. Kim and J. J. van Zyl, "A time-series approach to estimate soil moisture using polarimetric radar data," IEEE Trans. Geosci. Remote Sens., 47(8), 2519-2527 (2009).

60. N. Pierdicca, L. Pulvirenti, F. Ticconi, M. Brogioni, "Radar bistatic configurations for soil moisture retrieval: A simulation study," IEEE Trans. Geosci. Remote Sens, 46, 3252-3264 (2008).

61. M. Brigioni, S. Pettinato, G. Macelloni, S. Paloscia, P. Pampaloni, N. Pierdicca, and F. Ticconi, "Sensitivity of bistatic scattering to soil moisture and surface roughness of bare soils," Int. J. Remote Sens., 31(15), 4227-4255 (2010).

62. T. Li, I. Hajnsek and K.-S. Chen, "Sensitivity analysis of bistatic scattering for soil moisture retrieval," Remote Sensing, 13(2), 188 (2021).

63. D. Masters, S. Katzberg, and P. Axelrad, "Airborne GPS bistatic radar soil moisture measurements during SMEX 02," in Proc. IEEE Int. Geosci. Remote Sens. Symp., pp.896–898, 2003.